Comprehensive review of HALO, an high precision orbit propagation tool for mission design in the cis-lunar domain

Quentin Granier[12], Yang Yang[2], Andrew G. Dempster[1]

September 20, 2024

1. Australian Center for Space Engineering Research, School of Electrical Engineering and Telecommunications, UNSW, Sydney, NSW 2052, Australia

2. School of Mechanical and Manufacturing Engineering, UNSW, Sydney, NSW 2052, Australia

1 Abstract

With the recent implementation of the Artemis Accords, interest in the cis-lunar space is rapidly increasing, necessitating the development of more precise and accurate modeling tools. While general-purpose mission design tools are available, this study proposes an open-source mission design tool, HALO for High-precision Analyser for Lunar Orbits, specifically built upon a high-precision lunar orbit propagator, tailored for the cis-lunar environment. This work presents a comprehensive review of the modeling approaches, structural design, and algorithms employed, aiming at facilitating ease of use and adaptation for other research in the cis-lunar domain. Furthermore, accuracy studies of the propagator are provided for various orbits of interest within this domain, including low lunar orbits, elliptical frozen orbits, and 3-body problem orbits, such as Near Rectilinear Halo Orbits and Distant Retrograde Orbits.

Contents

1 Abstract **1**

2 Introduction **2**

3 Time and coordinate systems **3**
3.1 Time . . . 3
3.2 Frames . . . 4
3.2.1 J2000 - Integration frame . . . 4
3.2.2 Geopotential frames . . . 4
3.2.3 Earth-Moon rotational frame - 3BP orbits . . . 4

4 High fidelity ephemeris models **6**
4.1 Modelling of field forces . . . 6
4.1.1 Lunar gravitational field . . . 6
4.1.2 Lunar solid tides . . . 7
4.1.3 Point mass attraction . . . 7
4.1.4 Earth gravitational field . . . 7
4.1.5 General relativistic correction . . . 8
4.2 Modelling of surface forces . . . 8
4.2.1 Solar radiation pressure . . . 8
4.2.2 Earth albedo . . . 9
4.3 Considerations on implementation . . . 10
4.3.1 Implementation of the Lunar gravity field . . . 10

4.3.2 Lunar gravity field assessment . . . 13
4.3.3 Earth gravity field assessment . . . 13
4.3.4 Integration parameters choice . . . 14
4.3.5 Time and coordinate systems handling . . . 16
4.4 Summary of all forces . . . 16

5 Assessment of the propagator using real-life cis-lunar orbits 17
5.1 Process of assessments . . . 17
5.2 Low Lunar Orbit . . . 17
5.2.1 Reference orbit . . . 17
5.2.2 Magnitude of each perturbation . . . 18
5.2.3 Sensitivity analysis . . . 18
5.3 Elliptical Lunar Frozen Orbit . . . 19
5.3.1 Reference orbit . . . 19
5.3.2 Magnitude of each perturbation . . . 20
5.3.3 Sensitivity analysis . . . 20
5.4 Near Rectilinear Halo Orbit . . . 21
5.4.1 Reference orbit . . . 21
5.4.2 Magnitude of each perturbation . . . 21
5.4.3 Sensitivity analysis . . . 22
5.5 Distant Retrograde Orbit . . . 23
5.5.1 Reference orbit . . . 23
5.5.2 Magnitude of each perturbation . . . 24
5.5.3 Sensitivity analysis . . . 25
5.6 Sum up of the perturbations over all orbits . . . 25

6 Mission design 26
6.1 Lambert problem optimizer algorithm . . . 26
6.2 3BP Orbits optimization algorithm . . . 27

7 Conclusion 29

8 Acknowledgement 29
8.1 Declaration of competing interest . . . 29

9 References 30
9.1 Author biography . . . 31

2 Introduction

This study is situated within the framework of the Artemis Accords, initiated by the United States and endorsed by 43 parties globally, including Australia since its inception in 2020. These accords establish a framework for international collaboration in the civil exploration and peaceful utilization of extraterrestrial bodies and objects. The Accords were developed in conjunction with the National Aeronautics and Space Administration's (NASA) 2017 Artemis program, which involves a budget of US$100 billion and aims to return humanity to the Moon while advancing cis-lunar space exploration. Mastery of the cis-lunar domain is intended to establish a permanent human presence on the Moon and facilitate access to deep space, thereby advancing the future of global human exploration to Mars and beyond.

Recent years have witnessed the development of various projects in this domain, including the Gateway mission [1], the Artemis missions [2], and the Japan Aerospace Exploration Agency (JAXA) Lunar Navigation Satellite System (LNSS) [3]. These projects involve different orbits of interest within the cis-lunar domain. The Gateway mission intends to establish a lunar space station in a Southern Near Rectilinear Halo Orbit (NRHO) around the L2 Lagrange point, an orbit characterized by the gravitational interaction between the Earth and the Moon. The Capstone mission, launched in June 2022, was tasked with exploring this future lunar space station orbit [4]. Additionally, Artemis I, launched in November 2022, investigated the Distant Retrograde Orbit (DRO), another type of orbit

governed by three-body dynamics. Meanwhile, JAXA's LNSS is developing an efficient navigation and communication system around the Moon, utilizing Elliptical Lunar Frozen Orbits (ELFO). The lunar gravitational field, which is complex due to geological history and mass concentrations (mascons) [5], significantly affects orbits close to the Moon, often causing them to decay. Some orbits show periodic changes and are then called "frozen" orbits like the ELFO. Given the complexity of the lunar gravitational field, low lunar orbit (LLO) also warrants detailed study. This study will consider the four aforementioned orbits as reference points within the cis-lunar domain.

As previously discussed, the cis-lunar domain is governed by multiple complex forces, and the increasing interest in this area necessitates the development of lunar high-precision orbit propagators (LHPOP). Existing tools such as the Systems Tool Kit (STK from Ansys) and the General Mission Analysis Tool [6] (GMAT from NASA) are general-purpose software; although GMAT is open-source, modifications and precise modeling within it are not easily accessible. This study addresses the need for a specialized LHPOP tailored to lunar orbits, offering a comprehensive review of the modeling techniques, sensitivity analysis on cis-lunar domain orbits, and integration into a mission design tool with detailed algorithms named HALO for High-precision Analyser for Lunar Orbits. In addition to free propagation, HALO enables the resolution of mission design problems, such as the optimization of Lambert transfers or the convergence of three-body problem orbits from simplified circular restricted models to highly accurate ephemeris models. Figure 1 summarizes the key considerations of the study with a graphical table of content.

The remainder of this paper is organized as follows: Section II defines the temporal considerations and coordinate systems utilized. Section III discusses the models employed and the enhancements implemented. Section IV presents the accuracy and performance outcomes for the aforementioned orbits, and Section V introduces the mission design tool and the algorithms used, followed by concluding remarks and acknowledgements.

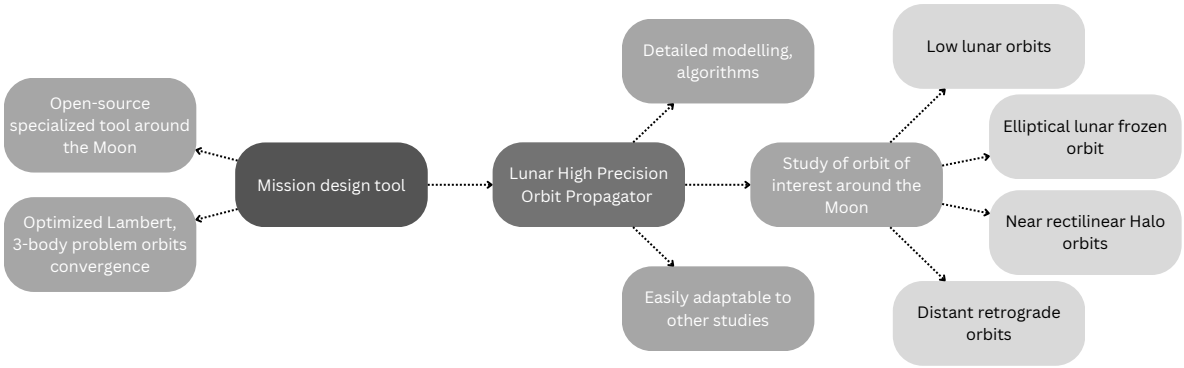

Figure 1: Graphical table of contents

3 Time and coordinate systems

Time and coordinate system considerations are crucial for any space-related application. The concept of time on Earth varies by time zone, depends on the Earth's rotational velocity, and is not continuous, with the second as the smallest unit. When factoring in general relativistic effects, it becomes necessary to establish a precise and universally applicable time reference by fixing a specific location and epoch and considering a continuous progression of time independent of physical influences. Similarly, while different orbits or forces may be best defined within specific reference frames, a common inertial frame is required to integrate the equations of motion. This section addresses the time and frame considerations necessary to establish a solid foundation for the subsequent analysis. More information on the implementation can be found in the respective section 4.3.

3.1 Time

When processing orbital calculation, one has to be more precise than the second and the discontinuous calendar time is not sufficient. To this extent, the Barycentric Dynamic Time (TDB) also referred to

as the Ephemeris Time (ET) can be used. The TDB would be the time kept by an atomic clock at the solar system barycenter. It is defined as the independent variable in the differential equation of motion of all solar system planets [7]. This number corresponds to the number of ephemeris seconds past J2000, so the seconds (and part seconds) elapsed if we were at the solar system barycenter. J2000 corresponds to the epoch of the 1st January 2000 at noon (12pm). It is important to note that this epoch is referenced in TDB and not in UTC, being the Earth time at Greenwich globally used in everyday life after consideration of the time zones. Those times are different (but really close) because of the relativistic effect and the leap seconds. The "leap seconds" are seconds added every once in a while to the UTC time so that the UTC noon matches the noon solar alignment.

3.2 Frames

3.2.1 J2000 - Integration frame

Considering a mission design tool, some forces or considerations can exist in different specific frames. For instance, the geopotential calculations for a specific body have to be done in a body fixed frame but the integration has to be done in an inertial frame of reference. Every force has then to be converted in the integration frame.

Usually we consider the J2000 frame as the reference frame for integration. This frame corresponds to the Earth's mean equator and equinox at the 1 Jan 2000 12pm TDB.

3.2.2 Geopotential frames

As mentioned before, in the computation of the gravity fields around a body, one has to consider the position of the spacecraft in a body-fixed frame. The propagator considers the gravity fields of two bodies, i.e., the Moon and the Earth, and the associated coefficients are defined in a specific frame.

For the Moon, the Moon Principal Axes (PA) frame is used. The principal axes are defined as the axes for which the Moon's inertia tensor is diagonal. They correspond to the axes around which the body tends to rotate.

For the Earth, the World Geodetic System 84 (WGS84) frame designed for the Global Positioning System is used. Some other International Terrestrial Reference Frames can also be used, such as the ITRF93 used in SPICE[1] (Spacecraft, Planet, Instrument, C-matrix and Events), which is aligned with the WGS84 to within less than 0.1m on Earth surface [8].

3.2.3 Earth-Moon rotational frame - 3BP orbits

The study of the special three body problem (3BP) orbits like the NRHOs or the DROs leads to the use of the Earth-Moon rotational frame. Indeed, those 3BP orbits can be computed in a simplified analytic model called the Circular Restricted 3 Body Problem, CR3BP. This model considers a circular motion of the Moon around the Earth and the equation are in the rotating frame following the movement of the Moon. This frame is defined by its center on the Earth-Moon barycenter, the x-axis pointing toward the Moon, the y-axis in the direction of the Moon's velocity and the z-axis orthogonal to the orbital plane.

In an inertial Moon centered frame like the integration frame, those axes can be represented respectively by u_R, u_θ and u_Z shown on Figure 2. Two main cases can lead to do a transition between the inertial frame and the rotational one. First of all, after the computation of a CR3BP solution, we would like to simulate the same initial state with our high precision propagator and we need to convert this initial state from a circular restricted model in the rotational frame to a precise ephemeris model in the inertial frame. The second case would be when we propagate our initial condition, all the computations are done in the integration frame, an inertial frame. We may then also want to visualise the resulting propagation in the rotational frame. The first case requires to fit the simplified model on an ephemeris model and then to convert to the inertial frame and the second case only requires to do the inverse conversion, without the fitting part.

Let us start by considering the first case, and the second one will derived from it. First of all, the CR3BP model being circular restricted, some assumptions have to be made in order to proceed to a

[1] SPICE will be introduced in the implementation section 4.3. It helps managing the time and frames related considerations

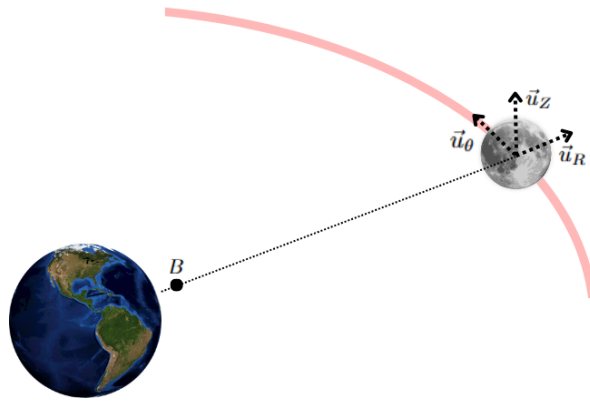

Figure 2: Definition of the rotational frame from the inertial one

fitting to an ephemeris model. The main body being the Moon, we can define that the Moon is at the same place in the two models, i.e., the CR3BP and the ephemeris models. Hence the Earth-Moon distance is fixed to an average lunar unit (LU) of $R_{LU} = 389703$ km. Therefore, the Earth cannot stay at the same position in both models. We define then the CR3BP Earth to be in the same direction as the ephemeris Earth but at a distance of R_{LU}. This allows us to compute the position of the barycenter B which is the center of the CR3BP coordinate system.

We will start by finding a relation between the E point (CR3BP Earth) and the B point (CR3BP Barycenter) from the barycentre equality:

$$m_M \vec{BM} + m_E \vec{BE} = \vec{0}, \tag{1}$$

$$\vec{ME} = \vec{MB} + \vec{BE} = \left(1 + \frac{m_M}{m_E}\right) \vec{MB} = \frac{1}{1-\mu} \vec{MB}, \tag{2}$$

where M is the Moon center, m_X is the mass of body X and $\mu = \frac{m_M}{m_M + m_E}$ is the ratio of mass. Therefore we can compute the position of the B point:

$$\vec{MB} = (1-\mu)\vec{ME} = (1-\mu) R_{LU} \frac{\vec{ME}_{\text{eph}}}{|\vec{ME}_{\text{eph}}|}, \tag{3}$$

where eph stands for ephemeris. Another fitting strategy is to consider a factor of $\cdot \frac{|\vec{ME}|}{R_{LU}}$ to scale the satellite state. According to our experimental results in this work the first fitting strategy in Equations (1-3) yields better performance. Hence, no scaling is used and the average Earth-Moon distance is used. Lastly, we logically fit the rotational axes on the u_R, u_θ and u_Z derived from the ephemeris Earth position with respect to the Moon:

$$\begin{aligned}
\vec{u}_R &= -\frac{\vec{ME}}{|\vec{ME}|} \\
\vec{u}_\theta &= -\frac{\vec{V}}{|\vec{V}|} \quad \text{with } \vec{V} = \frac{d\vec{ME}}{dt} \\
\vec{u}_Z &= \vec{u}_R \times \vec{u}_\theta
\end{aligned}$$

Now that the models are fitted, we can proceed to the conversion:

$$\begin{aligned}
\vec{MS}_{[I]} &= \vec{MB}_{[I]} + \vec{BS}_{[I]} \\
&= \vec{MB}_{[I]} + M_{RI} \cdot \vec{BS}_{[R]} \\
&= \vec{MB}_{[I]} + X_{[R]} \cdot \vec{u}_R + Y_{[R]} . \vec{u}_\theta + Z_{[R]} . \vec{u}_Z
\end{aligned} \tag{4}$$

$$\begin{aligned}
\vec{V}_{S/M[I]} &= \vec{V}_{S/B[I]} + \vec{V}_{B/M[I]} \\
&= \vec{V}_{S/B[RI]} + \vec{\Omega}_{R/I} \times \vec{BS}_{[I]} + \vec{V}_{B/M[I]} \\
&= M_{RI} \cdot \vec{V}_{S/B[R]} + \vec{\Omega}_{R/I} \times \vec{BS}_{[I]} + \vec{V}_{B/M[I]}
\end{aligned} \tag{5}$$

And $\vec{\Omega}_{R/I}$ is defined as follows:

$$\vec{\Omega}_{R/I} = \Omega_{R/I} \cdot \vec{u}_Z, \tag{6}$$

$$\frac{d\vec{u}_R}{dt} = \Omega_{R/I} \cdot \vec{u}_\theta, \tag{7}$$

with M the Moon, B the Barycenter, S the Spacecraft, [I] the inertial frame J2000, [R] the rotational frame, [RI] the frame with the same center as [R] but same axes as [I], M_{RI} the transition matrix from [R] to [I], (X, Y, Z) the coordinates of $\vec{BS}$, $\vec{V}_{S/M[I]}$ the velocity of S with respect to M in [I] and $\vec{\Omega}_{R/I}$ the rotational velocity between the two frames (expressed in [I]), defined in Equations 6 and 7. Equation 6 defines the vector's direction and Equation 7 defines the norm from the rotational unit vectors.

We can then now calculate the state in the inertial frame from the rotational one, with the previous conversion, and we can apply this process to our initial condition in order to propagate. As the fitting cannot be perfect, starting from a DRO or NRHO trajectory, the ephemeris trajectory is not a real DRO or NRHO anymore, but we have a good initial guess close to the solution to initiate a convergence algorithm. See Part 6.2 for further information.

We consider the second case now where we want to convert the trajectory from the inertial frame to the rotational one. To convert the whole trajectory, we have to apply this conversion to every point of the trajectory.

$$\begin{aligned} \vec{MS}_{[R]} &= M_{IR} \cdot \vec{MS}_{[I]} \\ &= M_{RI}^{-1} \cdot \vec{MS}_{[I]} \end{aligned} \tag{8}$$

$$\begin{aligned} \vec{V}_{S/M[R]} &= M_{IR} \cdot \vec{V}_{S/M[RI]} \\ &= M_{RI}^{-1} \cdot \left(\vec{V}_{S/M[I]} - \vec{\Omega}_{R/I} \vec{MS}_{[I]} \right) \end{aligned} \tag{9}$$

And M_{RI} is defined by u_R, u_θ and u_Z in column, similarly as in the first case. We kept the same notation

4 High fidelity ephemeris models

The cis-lunar domain is influenced by multiple forces, with their impact varying depending on a satellite's position. Certain orbits of interest, such as those described by the three-body problem, exist due to the delicate balance between the gravitational pulls of the Earth and the Moon. To study these orbits, it is necessary to develop a high-precision propagator, and in this section, all relevant forces in the cis-lunar domain will be modeled. Implementation considerations will also be discussed to ensure the accuracy of the propagator. The goal of this section is to provide a detailed understanding of the propagator's inner workings, facilitating its use in future studies. The propagator presented here builds on the work of Ennio Condoleo [9], which has been further refined, detailed, and integrated into a mission design tool. This section will present the modelling for all field and surface forces and will then present some useful implementation consideration.

4.1 Modelling of field forces

4.1.1 Lunar gravitational field

The assumption of an homogeneous gravity field for the Lunar gravity field is false. Thus the point mass model cannot be used. As a matter of fact, the Moon contains multiple "mascons" (mass concentration) unevenly distributed because of its past [5]. So the Moon's attraction depends on the relative position around the body. The gravity field potential is usually modelled in the body-fixed frame aligned on the Moon's principal axes (Moon PA frame) and the model uses the expansion in spherical harmonics (see [7] from page 56):

$$U = \frac{GM_\oplus}{r} \sum_{n=0}^{\infty} \sum_{m=0}^{n} \frac{R_\oplus^n}{r^n} P_{nm}(C_{nm}\cos(m\lambda) + S_{nm}\sin(m\lambda)), \tag{10}$$

With the following terms:

$$C_{nm} = \frac{2-\delta_{0m}}{M_\oplus} \frac{(n-m)!}{(n+m)!} \int \frac{s^n}{R_\oplus^n} P_{nm}(\sin\phi')\cos(m\lambda')\,\rho(s) d^3 s,$$
$$S_{nm} = \frac{2-\delta_{0m}}{M_\oplus} \frac{(n-m)!}{(n+m)!} \int \frac{s^n}{R_\oplus^n} P_{nm}(\sin\phi')\sin(m\lambda')\,\rho(s) d^3 s,$$

with P_{nm} being the Legendre polynomials, $\oplus$ corresponding to the Earth, δ being the Kronecker's symbol (1 if both index are the same, else 0) and ρ being the mass density at a given point. (r, ϕ, λ) and (s, ϕ', λ') correspond both to the spherical coordinates radius, latitude, longitude but different ones.

Given the potential, you can compute the acceleration in the form of the gradient of the potential. The coefficient C_{nm} and S_{nm} are processed during precise mission aiming at mapping the lunar geopotential like the GRAIL mission for the Moon [10].

The implementation of this force demands to take care of other considerations that will be discussed in section 4.3.

4.1.2 Lunar solid tides

The rotation of the Moon is almost exactly equal to its orbital period around the Earth which leads the Moon to always face the Earth. Thus the solid tides applied by Earth to the Moon will always be in the same direction in the Moon's body fixed frame. Solid tides are defined as tides that are applied to solid materials and thus are applied to any body like the Moon. Then for the Moon, solid tides become a static problem that can be considered in the calculations of the lunar gravitational fields parameters C_{nm} and S_{nm}.

It is then all the more important to choose the most accurate data for those coefficients in order to have the best accuracy on both the lunar gravitational field and the lunar solid tides.

4.1.3 Point mass attraction

When we consider orbits in the vicinity of the Moon, the bodies with the most influence are the Moon obviously, followed by the Earth, the Sun and then Jupiter and Venus. Even though Jupiter is further than Venus, its huge mass creates a bigger attraction on lunar orbits.

These bodies are considered as point masses when calculating their gravitational pulls. However, as opposed to the Moon, those additional bodies C are third body perturbation and they have an attraction on both the spacecraft S and the Moon M. The resulting perturbation can be written:

$$\begin{aligned} \vec{a}_{C/S[M]} &= \vec{a}_{C/S[J2000]} - \vec{a}_{C/M[J2000]} \\ &= -GM_\oplus \frac{\vec{r}_S}{r_S^3} - GM_\oplus \frac{\vec{r}_0}{r_0^3}, \end{aligned} \tag{11}$$

where $\vec{r}_S$ represent the vector from Earth to the spacecraft, and $\vec{r}_0$ represent the vector from the Moon to Earth. The notation "C/S" stands for "Body over Spacecraft". The geometry of Earth-Moon-Spacecraft is illustrated in Figure 3.

Equation 11 indicates that the third body perturbation on the spacecraft corresponds to the attraction force of the body on the spacecraft subtracted by the attraction force on the Moon.

4.1.4 Earth gravitational field

To consider the Earth gravitational field (EGF) in a Moon centered frame, we have to use the point mass model and turn it into a harmonic model:

$$\vec{a}_{E/S[M]} = -GM_\oplus \frac{\vec{r}_S}{r_S^3} - GM_\oplus \frac{\vec{r_0}}{r_0^3} \tag{12}$$

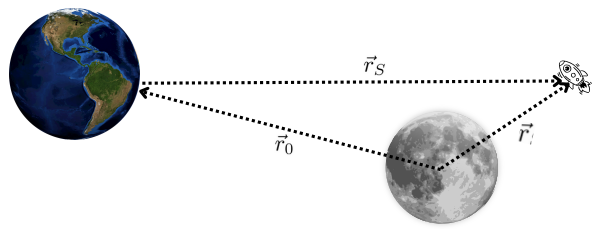

Figure 3: Third body perturbation - Vectors definition

With r_S the vector Earth-Spacecraft and r_0 the vector Moon-Earth.

So we just have to compute the 2 terms the same as the lunar gravitational field but with different C_{nm} and S_{nm} coefficients associated to the Earth. We have then:

$$\vec{a}_{E/S[M]} = A_{EGF}(\vec{r}_S) - A_{EGF}(-\vec{r}_0) \tag{13}$$

Where A_{EGF} is the gravitation field algorithm developed in section 4.3 from the Lunar gravitational model in section 4.1.1 but with Earth's coefficient.

4.1.5 General relativistic correction

The special relativity theory, that we usually use, considers a flat spacetime. But when the spacecraft is in the vicinity of a massive body, one as to take into account corrections related to the general relativity, the spacetime is bent. Indeed, the acceleration correction due to the general relativity can be expressed as in [7] from page 110:

$$\ddot{\vec{r}} = \frac{GM}{r^2}\left(\left(4\frac{GM}{c^2 r} - \frac{v^2}{c^2}\right)\vec{e_r} + 4\frac{v^2}{c^2}\left(\vec{e_r}\cdot\vec{e_v}\right)\vec{e_v}\right) \tag{14}$$

With c the celerity of light, $\vec{e_r}$ is the unit vector in the direction of $\vec{r}$ and $\vec{e_v}$ is the unit vector in the direction of $\vec{v}$.

4.2 Modelling of surface forces

4.2.1 Solar radiation pressure

The solar radiations creates a pressure on the spacecraft. To model it, we have the pressure model (taken from [7] page 77):

$$P = \frac{\Phi}{c}, \tag{15}$$

$$\Phi = \frac{L_s}{4\pi R_S^2}, \tag{16}$$

Φ is the total solar irradiance, c is the celerity of light in the void, L_s is the sun brightness power and R_S is the distance to the Sun. Thus, by considering a spherical shaped satellite and only the specular reflections, we obtain:

$$F = \frac{PAC_R}{m} \tag{17}$$

with F being in the opposite direction of the Sun. A is here the cross section of our satellite, assumed circular and C_R is the radiation pressure coefficient. C_R lies between 0 and 2, with 0 accounting for no reflection, 1 for a black body and 2 for a total reflection.

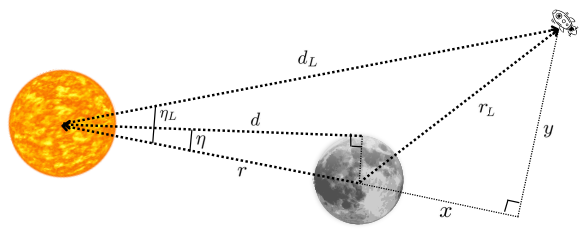

Figure 4: Eclipse condition

We just need to implement a condition of eclipse when the Sun does not see the spacecraft, which means the spacecraft is behind the Moon. All notations are defined in Figure 4. The condition of being hidden by the Moon is:

$$\begin{cases} |\eta_L| < |\eta| \\ d_L > d \end{cases} \Leftrightarrow \begin{cases} \cos(\eta_L) > \cos(\eta) \\ d_L > d \end{cases} \tag{18}$$

And with geometrical considerations (Figure 4), we have:

$$\begin{aligned} \cos(\eta) &= \frac{d}{r} \\ \cos(\eta_L) &= \frac{r+x}{d_L} \\ x^2 + y^2 &= r_L^2 \\ (x+r)^2 + y^2 &= d_L^2 \end{aligned} \tag{19}$$

We can now solve for x:

$$\begin{aligned} &x^2 + 2xr + r^2 + y^2 - (x^2 + y^2) = d_L^2 - r_L^2 \\ &2xr + r^2 = d_L^2 - r_L^2 \\ &x = \frac{d_L^2 - r_L^2 - r^2}{2r} \end{aligned}$$

Finally, we can express $\cos(\eta_L)$:

$$\begin{aligned} \cos(\eta_L) &= (r + \frac{d_L^2 - r_L^2 - r^2}{2r})/d_L \\ \cos(\eta_L) &= \frac{d_L^2 - r_L^2 + r^2}{2rd_L} \end{aligned} \tag{20}$$

Thus Equations 19 and 20 express the variables in Equation 18 and the eclipse condition is obtained from geometrical considerations.

4.2.2 Earth albedo

The bond Earth albedo corresponds to the electromagnetic energy reflected by the Earth from the Sun. We can then derive the Earth albedo perturbation from the solar radiation pressure.

We can then use the same eclipse condition, for the Earth this time, and the pressure received by the Earth will be:

$$P_E = \frac{L_s}{4\pi r_S^2 \cdot c} \tag{21}$$

With r_S being the distance Earth-Sun, the other notations remaining the same.

However, the solar flux hits Earth surface $4\pi R_T^2$ with an area of πR_T^2. If we average on one day, the Earth received flux is then $P_E/4$ at R_T from its center. Then by the inverse square law and by considering the albedo coefficient, we have the pressure on the satellite:

$$P = \frac{P_E}{4} C_{alb} \left(\frac{R_T}{d_L} \right)^2 \tag{22}$$

With d_L being the distance Earth-Satellite.

This model for albedo is really simple and lots of elements are not taken into account as the Earth area elements or angles to normal or cloud coverage. See [7] for more information. But the resulting acceleration is already really low as we can see in the forces summary subsection.

4.3 Considerations on implementation

4.3.1 Implementation of the Lunar gravity field

The coefficients are usually normalised (we add a bar on top: $\bar{C}_{nm}$) in order to keep the magnitudes from changing significantly, so we have to convert the equations:

$$\left\{ \begin{array}{c} \bar{C}_{nm} \\ \bar{S}_{nm} \end{array} \right\} = \sqrt{\frac{(n+m)!}{(2-\delta_{0m})\,(2n+1)(n-m)!}} \left\{ \begin{array}{c} C_{nm} \\ S_{nm} \end{array} \right\} \tag{23}$$

Thus we have also to consider the new resulting Legendre polynomial and the resulting form for the acceleration due to the LGF:

$$\bar{P}_{nm} = \sqrt{\frac{(2-\delta_{0m})\,(2n+1)(n-m)!}{(n+m)!}} P_{nm} \tag{24}$$

$$\ddot{\boldsymbol{r}} = \nabla \frac{GM_\oplus}{r} \sum_{n=0}^{\infty} \sum_{m=0}^{n} \frac{R_\oplus^n}{r^n} \bar{P}_{nm}(\sin\phi) \left(\bar{C}_{nm} \cos(m\lambda) + \bar{S}_{nm} \sin(m\lambda) \right) \tag{25}$$

To compute this acceleration, we have to consider two things, computing the Legendre polynomials efficiently and deriving the gradient in Cartesian coordinate from the spherical ones.

First of all, we have in source [7] page 66 recursion formulas to generate all the Legendre polynomials. However, we consider instead normalized polynomials, so we have to do the conversion[2].

Therefore:

$$\bar{P}_{nn} = \sqrt{\frac{(2-\delta_{0n})\,(2n+1)(n-n)!}{(2n)!}} P_{nn} \tag{26}$$

$$= \sqrt{\frac{2\cdot(2n+1)}{(2n)!}} \cdot (2n-1)\cos(\phi) P_{n-1,n-1} \tag{27}$$

$$= \sqrt{\frac{2\cdot(2n+1)}{(2n)!}} \cdot (2n-1)\cos(\phi) \cdot \bar{P}_{n-1,n-1} \cdot \sqrt{\frac{(2n-2)!}{2\cdot(2n-1)}} \tag{28}$$

$$= \sqrt{\frac{(2n+1)(2n-1)}{(2n-1)2n}} \cdot \cos(\phi) \cdot \bar{P}_{n-1,n-1}$$

$$= \sqrt{\frac{(2n+1)}{2n}} \cdot \cos(\phi) \cdot \bar{P}_{n-1,n-1} \tag{29}$$

[2] In addition, in the code (accelharmonic.m) we consider a different standard for the indexes of the polynomials, $n_C = n+1$ and same for m_C (C for "Code"). The index are shifted up once, so the equations after conversion are just one index different from the equation in the code, the same is done for the coefficient C_{nm} and S_{nm} because Matlab table index start at 1 and not 0.

We used in Equations 26 and 28 the two statements: $2-\delta_{0n}=2$ and $2-\delta_{0,n-1}=2$ which are only valid for $n>1$. The first terms of P_{nn} are then initialised from the value in [7]: $P_{00}=1$ and $P_{11}=\sqrt{3}\cos\phi$

Equation 26 derives from Equation 24, Equation 27 from the recursive Equation 3.23 in source [7]. With Equation 28 we return back to the "bar" polynomial and lastly with Equation 29 we simplify the equation, similarly as Equations 30 and 31 for the other cases.

$$
\begin{aligned}
\bar{P}_{n,n-1} &= \sqrt{\frac{2(2n+1)1}{(2n-1)!}}\cdot(2n-1)\sin(\phi)\bar{P}_{n-1,n-1}\cdot 1/\sqrt{\frac{2(2n-1)1}{(2n-2)!}} \\
&= \sqrt{\frac{(2n+1)}{(2n-1)(2n-1)}}\cdot(2n-1)\sin(\phi)\bar{P}_{n-1,n-1} \\
&= (2n+1)\sin(\phi)\bar{P}_{n-1,n-1} \qquad (30)\\
\bar{P}_{n,m} &= \sqrt{\frac{2(2n+1)(n-m)!}{(n+m)!}}\cdot\frac{1}{n-m}\left((2n-1)\sin(\phi)\bar{P}_{n-1,m}\sqrt{\frac{(n+m-1)!}{2(2n-1)(n-m-1)!}}\cdots\right. \\
&\quad \left.-(n+m-1)\bar{P}_{n-2,m}\cdot\sqrt{\frac{(n+m-2)!}{2(2n-3)(n-m-2)!}}\right) \\
&= \frac{1}{n-m}\left((2n-1)\sin(\phi)\bar{P}_{n-1,m}\sqrt{\frac{2(2n+1)(n-m)!(n+m-1)!}{(n+m)!\cdot 2(2n-1)(n-m-1)!}}\cdots\right. \\
&\quad \left.-(n+m-1)\bar{P}_{n-2,m}\cdot\sqrt{\frac{2(2n+1)(n-m)!(n+m-2)!}{(n+m)!\cdot 2(2n-3)(n-m-2)!}}\right) \\
&= \frac{1}{n-m}\left((2n-1)\sin(\phi)\bar{P}_{n-1,m}\sqrt{\frac{(2n+1)(n-m)}{(n+m)(2n-1)}}\cdots\right. \\
&\quad \left.-(n+m-1)\bar{P}_{n-2,m}\cdot\sqrt{\frac{(2n+1)(n-m-1)(n-m)}{(2n-3)(n+m-1)(n+m)}}\right) \\
&= \sin(\phi)\bar{P}_{n-1,m}\sqrt{\frac{(2n+1)(2n-1)}{(n+m)(n-m)}}-\bar{P}_{n-2,m}\cdot\sqrt{\frac{(2n+1)(n-m-1)(n+m-1)}{(2n-3)(n+m)(n-m)}} \\
&= \sqrt{\frac{2n+1}{(n-m)(n+m)}}\left(\sin(\phi)\bar{P}_{n-1,m}\sqrt{2n-1}-\bar{P}_{n-2,m}\cdot\sqrt{\frac{(n-m-1)(n+m-1)}{(2n-3)}}\right) \qquad (31)
\end{aligned}
$$

In addition, the derivative of the Legendre polynomials with respect to ϕ is computed in the same time from the obtained equations. The derivative is needed in the computation of the spherical gradient.

With those 3 equations we can compute all Legendre polynomials. If we consider the coefficient in a triangle $(n, m \leq n)$, the first equation allows to compute the diagonal (n,n), then the second equation allows to compute the second diagonal (just under, $(n,n-1)$) from the first one, and the last formula allows to compute any other term from the 2 above itself.

Finally, the gradient is computed. However, the formulas for the gravity potential are in the spherical coordinates and the propagator needs Cartesian input and output. So first, the conversion from Cartesian to spherical coordinates for the spacecraft is done and then the gradient is computed with spherical coordinates as follows[3]:

$$
\nabla U = \frac{\partial U}{\partial r}\hat{\mathbf{r}} + \frac{1}{r}\frac{\partial U}{\partial \phi}\hat{\boldsymbol{\phi}} + \frac{1}{r\cos\phi}\frac{\partial U}{\partial \lambda}\hat{\boldsymbol{\lambda}} \qquad (32)
$$

[3]Equations 33, 34, 35 can be found in the code (accelharmonic.m)

With the following terms:

$$\begin{aligned}
\frac{\partial U}{\partial r} &= \frac{\partial}{\partial r}\left(\frac{GM_\oplus}{r}\sum_{n=0}^{\infty}\sum_{m=0}^{n}\frac{R_\oplus^n}{r^n}\bar{P}_{nm}(\sin\phi)\left(\bar{C}_{nm}\cos(m\lambda)+\bar{S}_{nm}\sin(m\lambda)\right)\right)\\
&= GM_\oplus\sum_{n=0}^{\infty}\sum_{m=0}^{n}\frac{\partial}{\partial r}\left(\frac{R_\oplus^n}{r^{n+1}}\right)\bar{P}_{nm}(\sin\phi)\left(\bar{C}_{nm}\cos(m\lambda)+\bar{S}_{nm}\sin(m\lambda)\right)\\
&= -(n+1)GM_\oplus\sum_{n=0}^{\infty}\sum_{m=0}^{n}\frac{R_\oplus^n}{r^{n+2}}\bar{P}_{nm}(\sin\phi)\left(\bar{C}_{nm}\cos(m\lambda)+\bar{S}_{nm}\sin(m\lambda)\right) \qquad (33)\\
\frac{\partial U}{\partial \phi} &= \frac{\partial}{\partial \phi}\left(\frac{GM_\oplus}{r}\sum_{n=0}^{\infty}\sum_{m=0}^{n}\frac{R_\oplus^n}{r^n}\bar{P}_{nm}(\sin\phi)\left(\bar{C}_{nm}\cos(m\lambda)+\bar{S}_{nm}\sin(m\lambda)\right)\right)\\
&= \frac{GM_\oplus}{r}\sum_{n=0}^{\infty}\sum_{m=0}^{n}\frac{R_\oplus^n}{r^n}\frac{\partial}{\partial\phi}\left(\bar{P}_{nm}(\sin\phi)\right)\left(\bar{C}_{nm}\cos(m\lambda)+\bar{S}_{nm}\sin(m\lambda)\right) \qquad (34)\\
\frac{\partial U}{\partial \lambda} &= \frac{\partial}{\partial \phi}\left(\frac{GM_\oplus}{r}\sum_{n=0}^{\infty}\sum_{m=0}^{n}\frac{R_\oplus^n}{r^n}\bar{P}_{nm}(\sin\phi)\left(\bar{C}_{nm}\cos(m\lambda)+\bar{S}_{nm}\sin(m\lambda)\right)\right)\\
&= \frac{GM_\oplus}{r}\sum_{n=0}^{\infty}\sum_{m=0}^{n}\frac{R_\oplus^n}{r^n}m\bar{P}_{nm}(\sin\phi)\left(-\bar{C}_{nm}\sin(m\lambda)+\bar{S}_{nm}\cos(m\lambda)\right) \qquad (35)
\end{aligned}$$

Here the vector form $\hat{\boldsymbol{r}}$, $\hat{\boldsymbol{\phi}}$, $\hat{\boldsymbol{\lambda}}$ corresponds to the spherical unit vectors. Then in the following, $\hat{\boldsymbol{x}}$, $\hat{\boldsymbol{y}}$, $\hat{\boldsymbol{z}}$ correspond to the Cartesian unit vectors.

After that, we can convert back the computed gradient to obtain the Cartesian acceleration. For that, we can use geometrical considerations on the sphere or use a formulary for the conversion from spherical unit vectors to cartesian unit vectors[4]:

$$\begin{aligned}
\hat{\mathbf{r}} &= \frac{x\hat{\mathbf{x}}+y\hat{\mathbf{y}}+z\hat{\mathbf{z}}}{\sqrt{x^2+y^2+z^2}} = \frac{x\hat{\mathbf{x}}+y\hat{\mathbf{y}}+z\hat{\mathbf{z}}}{r}\\
\hat{\boldsymbol{\phi}} &= \frac{\left(x^2+y^2\right)\hat{\mathbf{z}}-(x\hat{\mathbf{x}}+y\hat{\mathbf{y}})z}{\sqrt{x^2+y^2+z^2}\sqrt{x^2+y^2}} = \frac{\left(x^2+y^2\right)\hat{\mathbf{z}}-(x\hat{\mathbf{x}}+y\hat{\mathbf{y}})z}{r\sqrt{x^2+y^2}}\\
\hat{\boldsymbol{\lambda}} &= \frac{-y\hat{\mathbf{x}}+x\hat{\mathbf{y}}}{\sqrt{x^2+y^2}}
\end{aligned}$$

And with geometrical consideration on the sphere, by considering the circular cut of the three dimensional sphere, parallel to the x,y plane and going through the point of interest, we have:

$$r\cos\phi = \sqrt{x^2+y^2}$$

[4]Depending on the standard, formulas can be in radius r, latitude ϕ and longitude λ, or in radius r, polar angle $\theta = \phi - \frac{\pi}{2}$ and azimuthal angle $\varphi = \lambda$. On unit vectors, the only change is then $\hat{\boldsymbol{\theta}} = -\hat{\boldsymbol{\phi}}$.

We can now calculate the gradient and convert it to Cartesian coordinates:

$$
\begin{aligned}
\nabla U &= \frac{\partial U}{\partial r}\hat{\mathbf{r}} + \frac{1}{r}\frac{\partial U}{\partial \phi}\hat{\boldsymbol{\phi}} + \frac{1}{\sqrt{x^2+y^2}}\frac{\partial U}{\partial \lambda}\hat{\boldsymbol{\lambda}} \\
&= \frac{\partial U}{\partial r}\frac{x\hat{\mathbf{x}} + y\hat{\mathbf{y}} + z\hat{\mathbf{z}}}{r} + \frac{1}{r}\frac{\partial U}{\partial \phi}\frac{\left(x^2+y^2\right)\hat{\mathbf{z}} - (x\hat{\mathbf{x}} + y\hat{\mathbf{y}})z}{r\sqrt{x^2+y^2}} + \frac{1}{\sqrt{x^2+y^2}}\frac{\partial U}{\partial \lambda}\frac{-y\hat{\mathbf{x}} + x\hat{\mathbf{y}}}{\sqrt{x^2+y^2}} \\
&= \left[\frac{x}{r}\frac{\partial U}{\partial r} - \frac{xz}{r^2\sqrt{x^2+y^2}}\frac{\partial U}{\partial \phi} - \frac{y}{x^2+y^2}\frac{\partial U}{\partial \lambda}\right]\hat{\mathbf{x}} \\
&\quad + \left[\frac{y}{r}\frac{\partial U}{\partial r} - \frac{yz}{r^2\sqrt{x^2+y^2}}\frac{\partial U}{\partial \phi} + \frac{x}{x^2+y^2}\frac{\partial U}{\partial \lambda}\right]\hat{\mathbf{y}} \\
&\quad + \left[\frac{z}{r}\frac{\partial U}{\partial r} + \frac{\sqrt{x^2+y^2}}{r^2}\frac{\partial U}{\partial \phi}\right]\hat{\mathbf{z}}
\end{aligned}
\tag{36}
$$

According to Equation 36, the acceleration due to the lunar gravity field is expressed with respect to the three Cartesian coordinates in the Moon PA frame.

Therefore this harmonic form allows us to consider a more precise gravity field than the point mass. In order to be the most accurate possible on the LGF, which is the dominant force, and on the lunar solid tides, we need the most accurate data for the C_{nm} and S_{nm} coefficients. The most accurate mission in this domain was the GRAIL mission [10] in 2012 with two spacecrafts GRAIL A/B working in pair to precisely compute the C_{nm} and S_{nm} coefficients. Those coefficients were then implemented into the propagator with a gravitational field model going up to 350x350 harmonics.

4.3.2 Lunar gravity field assessment

Now we want to study the accuracy brought by those new harmonics. We take the example of the LLO orbit. So based on Figure 6, we have that $a_{LGF} = 1.418763 \cdot 10^{-3}$ km/s^2 and the Earth albedo effect (the lowest perturbation) is on the order 10^{-16}.

We are going here to study the norm of the LGF for different harmonic numbers. It will then tell us the improvement of each harmonics compared to the reference LGF. The improvement compared to the previous harmonics (the difference in accuracy) is also shown.

Harmonic orders	(0,0)	(2,2)	(10,10)	(30,30)	(70,70)
Norm of LGF (km/s^2)	1.417777e-03	1.418120e-03	1.418604e-03	1.418674e-03	1.418763e-03
Improvement	Ø	3.4231e-07	4.8433e-07	6.9740e-08	8.9285e-08
Harmonic orders	(100,100)	(150,150)	(200,200)	(250,250)	(350,350)
Norm of LGF (km/s^2)	1.418759e-03	1.418759e-03	1.418759e-03	1.418759e-03	1.418759e-03
Improvement	3.7071e-09	4.6582e-10	7.9744e-12	9.3311e-14	1.1055e-14

Table 1: Improvement of the LGF with respect to the orders of harmonics

On Table 1, we observe that with 70 harmonics, the error is of order 10^{-9} (sum of the remaining errors) and of order 10^{-11} for 150 harmonics. Given the norm of all other forces, and the computing time (27.0s for 70x70 and 66.5s for 150x150 in LLO[5]), we will use 150x150 harmonics for all propagations in this work, as using more would require excessive computing time. Even though this result is based on a single orbit, we assume it is generally applicable.

4.3.3 Earth gravity field assessment

Similarly as for the lunar gravity field, we chose here the EGM2008 file for Earth coefficients, widely used for the Earth gravitational field. Now we are going to do the same study on the harmonics accuracy as for the LGF. Let's take the example of the LLO orbit, we have $a_{EGF} = 1.8465 \cdot 10^{-8}$ km/s^2 and the albedo effect (the lowest perturbation) is on the order 10^{-16}.

[5]This computing time is just informative and was obtained with a medium computer Intel Core i5 11^{th}G

So we are going to study the difference over different harmonic numbers between the norm of the EGF and the norm of the point mass Earth attraction (EPM). It will then tell us the improvement of each harmonics compared to the reference Earth attraction. We also show the improvement compared to the previous harmonics (the difference in accuracy).

Harmonic numbers	(0,0)	(2,2)	(3,3)	(10,10)	(100,100)
$\|\vec{a}_{EGF} - \vec{a}_{EPM}\|(km/s^2)$	1.0641e-21	1.6227e-14	1.6230e-14	1.6230e-14	1.6230e-14
Improvement	Ø	1.6227e-14	3e-18	$<$ 1e-19	$<<$ 1e-19

Table 2: Improvement of the EGF with respect to the number of harmonics

From Table 2, it is seen that the 0x0 harmonic is of order 10^{-21} which means that the EGF is equal to the point mass EGF, which was expected. Also, already with 3x3 harmonics, the improvement of the perturbation is lower that the lowest force taken into account (order of 10^{-16}). Moreover, in LLO, the computing time for 0x0 and 3x3 is roughly the same: 65-69s. So there is no need to use orders higher than 3x3.

Similarly to the LGF, even if it is only for one orbit, this result should be generally applicable.

4.3.4 Integration parameters choice

In addition to the pure modelling of forces and perturbation, the integrator's selection and the choice of parameters reveals to be of prime importance in the propagator's accuracy on some orbits. Different kind of integrators will then be compared in this section.

To compare integrators, we considered the propagation of the Lunar Reconnaissance Orbiter (LRO) spacecraft in LLO around the Moon for 4 days, with a period every 2 hours. Hence the orbital evolutional errors overall multiple revolutions can be assessed. Moreover, the integration choice have a big impact on the LLO orbit (Cf section 5.6) which is interesting for this study.

So for every integrator, the position root mean square error (RMSE) on a 4-day propagation in LLO are compared with respect to the tolerances. There is two types of tolerances. The relative one is a measure of the error relative to the size of each solution component, and the absolute one is a threshold below which the value of the ith solution component is unimportant. For our purpose, the absolute tolerance turned out to change nothing in the accuracy so it was fixed to 10^{-14} and only the relative tolerance was studied. The original relative tolerance was 10^{-6} in [9].

For our high fidelity purpose, we need an integrator with high accuracy, so we considered all the related kind of integrator from the Matlab ODE suite [11]. We then chose 4 integrators from this suite, the Matlab ODE45, the Matlab ODE78, the Matlab ODE89 and the Matlab ODE113. The first 3 integrators use the Runge-Kutta (RK) method and the name "ODE" is followed by two numbers nm, $m > n$. They correspond to an integrator of order m, so an error in h^{m+1}, and the computational error is processed from the difference with an order n. This computational error is used notably for step size control, the integration step size change depending on the computed error. ODE45 uses the Dormand-Prince RK45 formula [12], the ODE 78 and 89 are from the Verner's RK formulas with the 89 being more robust and the 78 being more efficient [13]. Finally, the ODE113 is a variable step and variable order method using the Adam-Bashforth-Moulton algorithm with orders varying between 1 and 13 [14].

The following table will present the RMSE of the 4 integrators for the propagation of the LRO on the 1st february 2020. For each value, the computing time with a medium computer Intel core i5 11^{th}G is also shown to give an insight of the complexity.

On Table 3, we colored in blue the combination integrator/relative tolerance (RT) that was chosen in the initial work. It can be seen that on this specific orbit, the choice yields a huge RMSE. The 4 red numbers are the 3 lowest values on the table in addition to the lowest value for the ode45. The first interesting thing is that all integrators with sufficiently low tolerance reach the same level of accuracy which is approximately 422m in this situation. By considering 1% error, ODE45 reaches this stage with a RT of 10^{-9}, ODE78 with 10^{-11}, ODE89 with 10^{-8} and ODE113 with 10^{-8}. ODE45 and ODE113 are then the fastest solver to reach this final value in around 95s.

However, some values (the other three in red) obtained with less computing time have similar (and even better) accuracies. This way, we would like to know if those low values are just positive

Relative tolerance, 10^{-n}	6	7	8	9	11
ODE45 RMSE (m)	26758	645.0	729.8	421.1	422.2
Computing time (s)	19.4	36.4	63.3	97.7	236.3
ODE78 RMSE (m)	5255	20901	1092	381.9	422.0
Computing time (s)	29.4	44.8	66.8	97.2	190.2
ODE89 RMSE (m)	175.6	363.9	419.3	422.8	422.3
Computing time (s)	64.1	91.2	126.8	169.6	300.3
ODE113 RMSE (m)	3150	291.9	418.9	425.3	422.4
Computing time (s)	40.8	64.0	92.9	129.5	206.4

Table 3: Integrators computing time and accuracies

integration errors or if those combinations of parameters are in general better choices. To this extent, we will test the 4 red combinations on an other epoch, the 6 February 2020.

	RMSE (m)	Computing time (s)
ODE89, RT 10^{-6}	682.5	66.3
ODE89, RT 10^{-7}	622.5	90.6
ODE113, RT 10^{-7}	269.6	62.1
ODE45, RT 10^{-9}	605.4	96.1

Table 4: Best combination on 6 Feb 2020

On Table 4, the ODE45 result gives use the stable final value for this situation which is 605.4m of accuracy. We can then see that the 2 ODE89 combinations become close but bigger than the ODE45 one, so that they were only positive integration errors on table 3. However, the ODE113 is still the fastest and most accurate one in this situation. To confirm the choice of ODE113 over ODE45, we consider a last situation on 10 March 2020.

	RMSE (m)	Computing time (s)
ODE113, RT 10^{-7}	147.6	67.4
ODE45, RT 10^{-9}	509.7	102.8

Table 5: Comparison between two combination candidate

In a third situation (Table 5), ODE113 is still giving a better result than the stable value that can be reached after longer processing time. However, even though this combination gives really good results, it is less stable than the ODE113/RT=10^{-8} combination. The stability is exemplified in the following Table 6.

	Reference RMSE (m)	w/o albedo RMSE (m)
ODE113, RT 10^{-7}, 01/02/2020	292	53
ODE113, RT 10^{-7}, 06/02/2020	270	399
ODE113, RT 10^{-8}, 01/02/2020	419	364
ODE113, RT 10^{-8}, 06/02/2020	566	595

Table 6: Stability of the new combination

The Earth albedo is the lowest perturbation in the LLO with an order of 10^{-16} so removing it should not perturb the results too much. However, with ODE113/10^{-7} we have really good RMSE but a very important variation when removing the Earth albedo compared to ODE113/10^{-8}. This observation can be linked to section 5.6 that shows that the LLO and ELFO are orbits where integration have a big impact, because the situation is more complex. Therefore, the choice of integrator will still be ODE113 because of the better results in accuracy and time efficiency, but the relative tolerance will be set to 10^{-8} for complex orbits, such as LLO and ELFO, while it will be set to 10^{-7} for other orbits.

In summary, this section studies different types of integrators with different configurations and force models. Due its overall performance on accuracy and run time, ODE113 is selected among others for the following assessments, the relative tolerance of which will be used according to the rule expressed above.

4.3.5 Time and coordinate systems handling

This mission design tool uses the help of SPICE to help to manage frames, time and get ephemeris positions of planets and spacecraft. SPICE, which stands for "Spacecraft, Planet, Instrument, C-matrix, Events" is an Observation Geometry System for Space Science Missions developed by the NAIF (the Navigation and Ancillary Information Facility) for the NASA [15].

SPICE is available for multiple language but we will use it in MATLAB and its third party version in python build with exactly the same standards. For Matlab, the use of SPICE is allowed by downloading Mice (see README) and by downloading and importing the spiceypy library in Python. The same SPICE functions can be used in all languages, with Matlab the function will have the prefix *cspice_* and in python the prefix *spiceypy*. Example: $cspice_furnsh(\text{"}naif0012.tls\text{"})$ and $spiceypy.furnsh(\text{"}naif0012.tls\text{"})$. From now on, only the SPICE function will be given and the good prefix has to be added to it to use the function.

We mainly use SPICE for the 3 following purposes. First of all, we want to be able to convert a date from UTC calendar time to ephemeris time (ET). In order to do so, SPICE needs to take into account "leap seconds" that are added every once in a while to have the UTC noon match the noon solar alignment. To do so, we have to load a file storing the dates of change: $furnsh(\text{"}naif0012.tls\text{"})$. In the Matlab propagator, all useful files are loaded in the same time at initialisation with a metakernel.tm file: $cspice_furnsh(\text{"}metakernel.tm\text{"})$. Then, in Matlab $cspice_str2et(t)$ is used to convert a UTC string time t = [yyyy month dd hh:mm:ss.-] to ET. And in Python, $spiceypy.datetime2et(spiceypy.datetime(y, m, d, h, m, s))$ is used.

The second purpose is to access the ephemeris of a planet or spacecraft. For that we have to load the specific data. This can be done with a .bsp file that encode the position of all planets and important body of the solar system, like with $furnsh(\text{"}de430.bsp\text{"})$. Or if the NAIF provides the data of the spacecraft that we want to study (list here: [16]), we load the corresponding file like $furnsh(\text{"}LRO_ES_90_202003_GRGM900C_L600.bsp\text{"})$. Then we can access the position with the function $spkezr(TARG, ET, REF, ABCORR, OBS)$, with TARG the target, ET the ephemeris time, REF the reference frame, usually "J2000", ABCORR the Aberration correction flag usually a empty string for no correction, OBS the observer or the reference. More details with the SPICE documentation.

Finally, we also want SPICE to handle the frames transition efficiently. Different SPICE functions allow to compute the transition matrix between two frames. There is $pxfrm2$, $sxform$, $pxform$ ... depending on the input arguments. Further details can be found with the SPICE documentation. Those functions should be used whenever possible for efficiency and simplicity reasons.

4.4 Summary of all forces

Here are then all the forces and perturbations taken into account by the propagator

1. Lunar gravity field - 350x350 harmonics model from the GRAIL mission
2. Earth gravity field - 100x100 harmonics model EGM2008
3. Sun and Jupiter point mass
4. Solar radiation pressure
5. General relativistic correction
6. Earth albedo

In conclusion, this section details the development of the modeling framework utilized for our high-fidelity propagator. Some perturbations, such as lunar radiation pressure and the gravitational influence of other planets in the solar system, were not further developed within this model due to their

negligible impact relative to the primary perturbations considered. To enhance the accuracy of the propagator, the recommendations provided in the preceding relevant section or the general guidelines in section 5.6 may be followed.

5 Assessment of the propagator using real-life cis-lunar orbits

5.1 Process of assessments

It is essential to assess whether modifications made to the propagator result in measurable improvements. To this extent, we compare its propagation to real existing trajectories. So it means that we take a real initial position of some spacecraft in an orbit of interest and we propagate it while comparing the propagation to the real data every 30s.

We chose the 4 following orbits to assess the propagator: LLO, ELFO, NRHO and DRO.

5.2 Low Lunar Orbit

5.2.1 Reference orbit

The LLO is commonly defined as the orbits under 100km of the Moon's surface (or around). Those orbits are of main interest around the Moon because it allows to study the surface in order for instance to map the gravitational field or study the lunar geology and it also allows a quick access for landing.

A property of these orbit are the high instability. Indeed, the lunar gravitational field is really complex because of the "mascons" and without further study on the initial position a spacecraft would crash into the lunar surface after some weeks. There are few stable orbits that prevent from the use of frequent maneuver burns, they are called frozen orbits.

The Lunar Reconnaissance Orbiter (LRO) is currently around the Moon since 2009 in a frozen polar orbit, so it only demands yearly maneuvers [17]. This spacecraft will be our reference for the LLO. The epoch we are going to consider is the 1st Feb 2020 and the span is 4 days which corresponds to multiple periods of around 2 hours each. The periselene on this period is 60km and the aposelene is 130km with an average of 95km so it can be considered a LLO. The computing time on a medium computer with Intel core i5 11^{th}G for this propagation is 64s and the initial integration time-step was set to 30s. The latter changes due to the step size control.

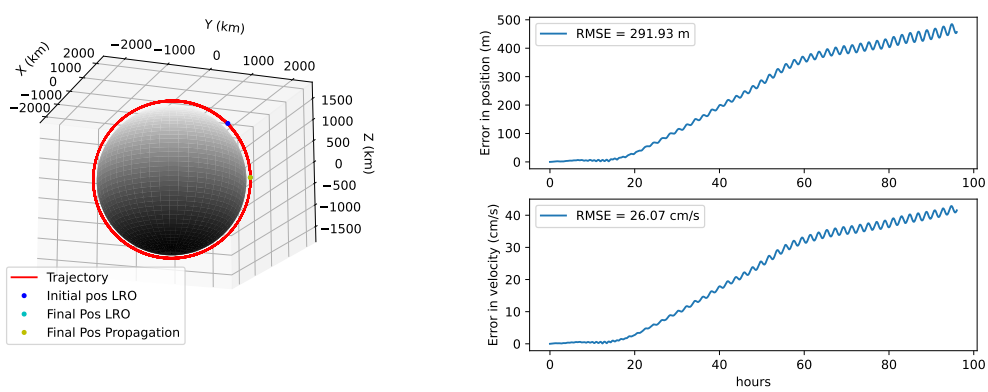

(a) Propagation in Low Lunar Orbit

(b) Error compared to the LRO

Figure 5: Propagation errors in LLO

On Figure 5a, we cannot see the cyan dot because it is on the same location as the green one, and we can see on Figure 5b that after 4 days the RMSE in position is 292m. This will be our reference for following modelling assessments for the propagator.

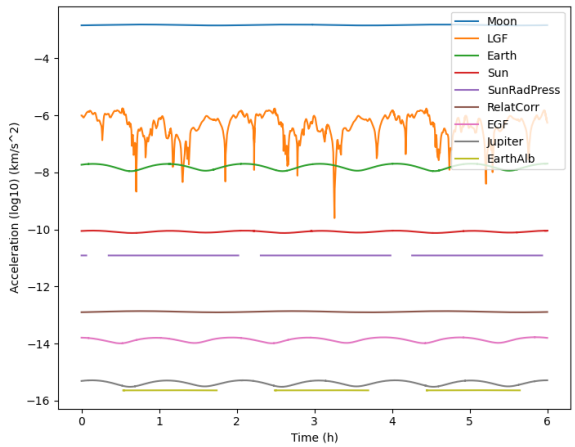

Figure 6: Magnitude of perturbations during a LLO

5.2.2 Magnitude of each perturbation

In Figure 6, we can see all the perturbations applied to the satellite and their amplitude. The span is 6 hours so around 3 orbits in LLO.

We are in low lunar orbit so we were expected to see a predominance of the lunar attraction (Moon on the graph), which is almost constant because the amplitude of the variation is only 70km, small compared to the Moon's radius.

The second predominant perturbation (overall) is the improvement of the lunar gravity field from the point mass (LGF on the graph). We can see here the results of the mascons that induce improvements for some position greater that others. We can see a periodicity for instance at t=2h and t=4h, there is the same evolution of the gravity field improvement.

Then the second most prominent body in this orbit is the Earth. We observe more fluctuations here than for the Moon even if the Earth is further away, it is due to the definition of the third body perturbation, see section 4.1.3. The Earth attraction is defined by a difference between the attraction on the spacecraft and the attraction on the Moon, so that when the spacecraft moves closer to the Moon, the difference tends to go to 0. We remark that the EGF improvement is way more stable than the LGF one because we only use 3 harmonics instead of 150 for the Moon.

Then we have the Sun attraction, the solar radiation pressure with some eclipse periods on the trajectory. The gaps in some functions are eclipse phenomena because the SRP and Earth albedo become null on specific occasion, see section 4.2.1. Then really low, we have still the relativistic corrections, the EGF improvement, Jupiter's attraction and the Earth albedo with also eclipse periods.

This figure helps us to consider which perturbation are predominant on the orbit. The graph can help to put focus on the improvement of certain perturbations or to know which to remove without losing too much accuracy and then winning computational power.

5.2.3 Sensitivity analysis

In this section, we are going to remove each perturbation or improvement made and assess the propagator in order to tell what is the relative role of each. Every other perturbation or improvement being similar to the reference.

As a remainder, the reference situation is an LLO on 4 days with 150x150 LGF harmonics, 3x3 EGF harmonics, the Sun attraction, an SRP coefficient of 1.3, the GR correction, the Jupiter attraction, an Earth albedo coefficient of 0.3, the integrator ODE113 and a relative tolerance of 10^{-8}.

	Reference	10x10 LGF	w/o Earth	w/o Sun	w/o SRP	w/o GRC
RMSE (m)	418.9	4548	814.7	387.6	377	389.2
	0x0 EGF	w/o Jupiter	w/o Albedo	ODE45 (RT=10^{-7})	RT of 10^{-6}	
RMSE (m)	408.5	441.2	363.7	602	2999	

Table 7: Relative role of each perturbation or improvement

With Table 7, we can see that when removing the perturbations with small impact, the result is close to the reference, such as without the GRC, with Earth point mass (i.e. 0x0EGF), w/o Jupiter's pull or w/o Earth's albedo. The value can be a bit lower than the reference due to positive integration mistakes because the orbit is known to have a complex integration. Indeed, the two last parameters correspond to the integrator's parameters and have a prime importance in this orbit. Therefore, the Earth albedo is on Figure 7 the smallest force but has 13% difference with the reference, so that it can be considered a positive integration mistake. Overall we can see that the biggest improvement is the LGF harmonics then the relative tolerance and the Earth attraction, the other are pretty small. We can also observe a lot of value under the reference which should not happen because it would mean that removing a perturbation improves the accuracy and then that the model for this perturbation is wrong. However this has to be compared with the other orbits and the difference with the reference is relatively low so that it can be considered instead as integration errors.

5.3 Elliptical Lunar Frozen Orbit

5.3.1 Reference orbit

The ELFO is an orbit around the Moon with a high eccentricity, with a big difference between the perilune and apolune. In addition the term "frozen" states that the orbit should maintained over time and require really low maintenance burns, and this is no easy task because of the very complex lunar gravitational field, similarly to the LLO. ELFO are then recognized by their periodicity in the change of their orbital elements so that it remains stable for a long time.

ELFO have been selected by JAXA as the best Lunar Navigation Satellite System (LNSS) orbit, an efficient navigation and communication system around the Moon that is currently developed [3]. However, there is not yet a satellite flying in this type of orbits. Therefore, in order to assess our propagator on such an orbit, we are going to focus on a slightly different orbit that flew, the Elliptical Polar Orbit (EPO). In particular, the Clementine spacecraft launched in January 1994 went into such orbit to perform a -60°/60° imagery and altimetry mapping of the Moon [18]. During the mapping period, 2 maneuver burns were performed, the second one on 11 April with the end of mapping on 22 April. We then chose the epoch 15 April 1994 at 3pm, to avoid the maneuver, and a span of 15hours to comprise 3 periods of 5 hours each. This date and span were chosen to avoid the discontinuities between the orbit determination tracks around every 20 hours. The perilune is 415 km and apolune is 2939 km. Finally, the computing time on a medium Intel Core i5 11^{th}G computer is 2.27s for an RMSE accuracy of 24.7m. The initial integration step size before the step size control was of 60s.

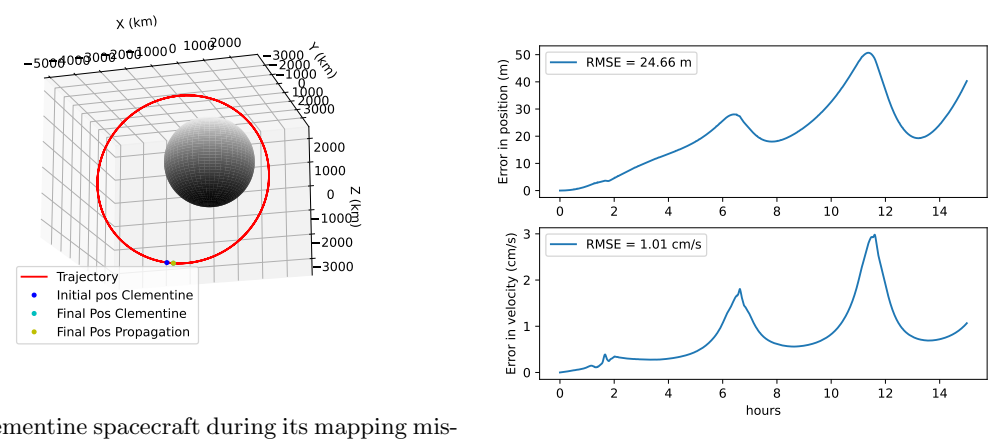

(a) The Clementine spacecraft during its mapping mission

(b) Propagation errors with Clementine

Figure 7: Propagation errors in an elliptical polar orbit

In the Figure 7a, we can see the polar orbit of the Clementine spacecraft during the second part of its mapping mission. The propagator is pretty accurate after 15 hours with around 20m error at apolune. We can see on Figure 7b that the velocity error goes up at perilune where the velocity is higher and that also create greater position error but it is expected from the geometry of the orbit.

5.3.2 Magnitude of each perturbation

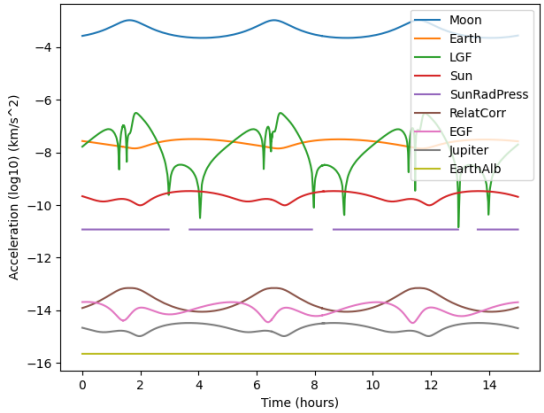

Figure 8: Magnitude of perturbations during a ELFO

In Figure 8, we study the accelerations over 3 periods and we observe a periodic motion as expected. The altitude varies a lot in the orbit but we are still completely in the Moon's SoI which is around 65 000 km. We can see as expected a dominance of the Moon attraction force, with some oscillations, with high LGF improvements that also vary significantly (due to the complex gravitational field described with 150 harmonics). Then we see the Earth, Sun and SRP and the other perturbations are really small similarly to the LLO orbit. We can also observe a minimum in the third body perturbations (Earth, Sun, Jupiter) when there is a maximum for the Moon attraction force. As discussed previously for the LLO orbit, this is because of the expression of the perturbation with a difference that comes close to 0 close to the Moon.

We also observe eclipse periods on the SRP when the spacecraft is covered by the Moon from the Sun.

5.3.3 Sensitivity analysis

In this section, we will systematically remove each perturbation or improvement and assess the propagator to determine the relative contribution of each, similarly with the LLO. All other perturbations or improvements will remain consistent with the reference situation.

As a remainder, the reference situation is an EPO on 15 hours and the model parameters are the same as for the LLO in section 5.2.3, except for the relative tolerance, which was set to 10^{-8}.

	Reference	10x10 LGF	w/o Earth	w/o Sun	w/o SRP	w/o GRC
RMSE (m)	24.7	61.0	2361	57.3	23.1	24.7
	0x0 EGF	w/o Jupiter	w/o Albedo	ODE45 (RT=10^{-7})	RT of 10^{-6}	
RMSE (m)	24.7	24.7	24.7	32.7	349	

Table 8: Relative role of each perturbation or improvement

With Table 8, we can see that removing a perturbation reduces the accuracy (and increases the RMSE) except for one small anomaly without the SRP. This may be due to an integrator positive mistake similarly with the LLO or maybe shows a problem in the modelling as we will discuss in the sum up part 5.6.

We can observe that only the Earth attraction and the relative tolerance have a big impact on this orbit, and then the improvement of the lunar gravity field and the Sun. This is what we could expect of an orbit a bit further from the Moon compared to LLO and so a bit closer to the Earth and Sun. The relative tolerance impact can be explain by the integration complexity of the orbit as we discussed earlier and in section 5.6.

5.4 Near Rectilinear Halo Orbit

5.4.1 Reference orbit

The NRHO is one of the star orbits of the decade and is the center of many studies for future missions or even space stations.

The NRHO is part of the halo orbits which are special orbits defined in the three-body problem and not the usual two-body problem for which the solution is an ellipse. Around the Moon, we can consider the spacecraft and the Moon for a two-body consideration but we can also add the Earth attraction and still obtain an precise analytic model. However, the halo orbits are defined in the circular restricted three body problem CR3BP, which is a simplified analytic model that allows their exact computation.

If an observer on Earth looks at a spacecraft in a halo orbit around the Moon, he will see a periodic motion which seems like a halo around the Moon. It means that the Halo orbits are periodic in a Moon centered rotational frame for the Earth-Moon system. The interest is then that whatever the movement of the Moon around the Earth, the relative position of the orbit to the Earth will be the same. The spacecraft can have always direct contact to the Earth which is perfect for communication.

The NRHO is a special kind of halo orbits that comes really close to the Moon's surface allowing easy access to the Moon. However, NRHO orbits are not the most stable orbits and periodic corrections are needed. An NHRO was then chosen by NASA for its lunar space station Gateway [1] and the spacecraft CAPSTONE was sent to discover the chosen NRHO [4]. This spacecraft will then be our reference for the NRHOs. The Capstone NRHO is in a 9:2 synodic resonance, thus the spacecraft traveled 9 periods around the Moon when the Moon finishes its second orbit around the Earth. We chose the epoch 25 November 2022 and a span of 6.5 days which is close to the average period of the NRHO of 6.68 days. The perilune is 1638 km and apolune is 69 083 km in altitude. Finally, the computing time on a medium Intel i5 computer is 1.2s for an RMSE accuracy of 1443m. The initial integration step size before the step size control was of 60s.

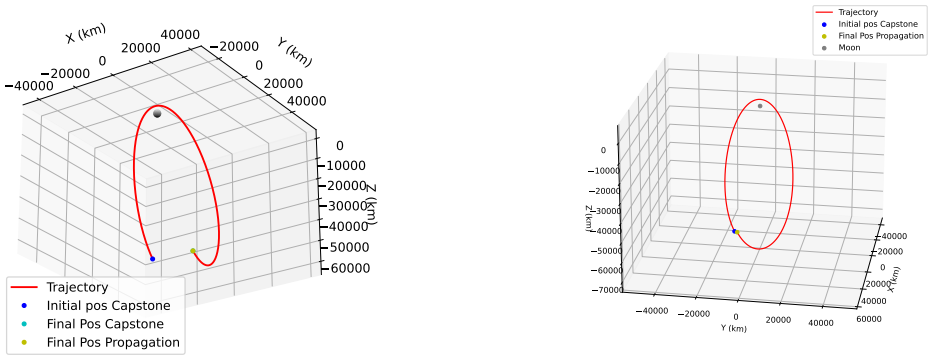

(a) Moon centered initial frame

(b) Moon centered rotational frame

Figure 9: CAPSTONE trajectory

In Figure 9a, the frame is the inertial (J2000) Moon centered which means that Earth turns around the Moon so does the orbit which is then not closed. However, in Figure 9b, the orbit is closed and we are in the Moon centered rotational frame so that Earth is fixed in this frame at around -400 000 km.

On Figure 10, we can see that the velocity error goes up significantly close to the Moon but it is relative to the absolute velocity that also increases.

5.4.2 Magnitude of each perturbation

In Figure 11, we study the accelerations over 1 period. The spacecraft goes really close to the Moon then back so that it explains the peak in the lunar attraction evolution. Moreover at apolune so 70 000 km, we are on the edge of the Moon's SoI, so that the attraction of the Earth and the Moon are

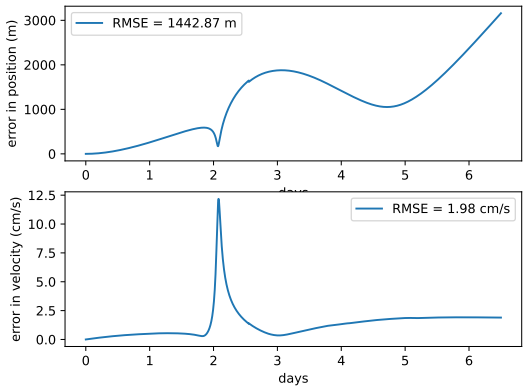

Figure 10: Propagation errors with CAPSTONE

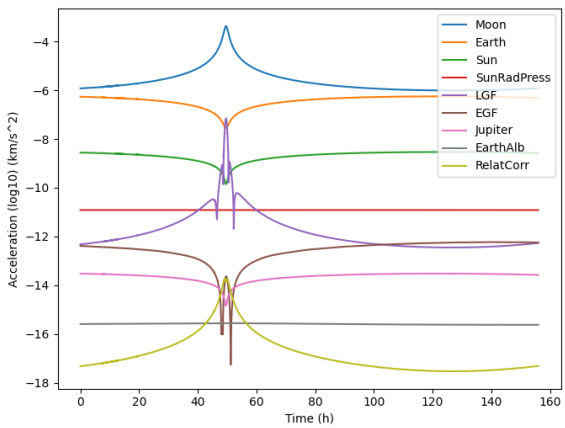

Figure 11: Magnitude of perturbations during a NRHO

almost equal. Also, close to the Moon, the Earth attraction perturbation gets closer to 0 because it is defined as the acceleration on the spacecraft minus the acceleration on the Moon. Therefore, close to the Moon, those 2 parts tends to become the same. We can also see the same for the Sun and Jupiter.

The SRP does not change much because it depends on the distance to the Sun which does not change too much. Same with the Albedo with the Earth because the NRHO is orthogonal to the Earth-Moon line so that the Earth to spacecraft distance does not change much.

For the gravity field improvements (LGF and EGF), we see an evolution similar to the norm of the acceleration so the bigger the force the bigger the improvement and we have some irregularities due to the harmonics. But the LGF is much lower than for the LLO as expected.

Finally, the relativistic correction is important only when the spacetime is bend so close to the Moon. We can see here that the 3 last perturbations are irrelevant as they are very low.

5.4.3 Sensitivity analysis

In this section, we are going to remove each perturbation or improvement made and assess the propagator in order to be able to tell what is the relative role of each. Every other perturbation or improvement is similar to the reference.

As a remainder, the reference situation is a NRHO on 6.5 days and the model parameters are the same as for the LLO in section 5.2.3, except for the relative tolerance, which was set to 10^{-7}.

In Table 9, the error for the integrator's choice is less important than the reference. This may mean that the choice of ODE113 over ODE45 for the NRHO was not the best choice but the impact is so small that it may just be an integrator positive mistake on this specific orbit (error $< 4\%$). Overall we can see that the biggest improvement is due to the Earth attraction then the Sun and the SRP, the

	Reference	10x10 LGF	w/o Earth	w/o Sun	w/o SRP	w/o GRC
RMSE (km)	1.443	1.443	10 307	93.0	1.776	1.443
	0x0 EGF	w/o Jupiter	w/o Albedo	ODE45 (RT=10^{-7})	RT of 10^{-6}	
RMSE (km)	1.435	1.484	1.443	1.404	2.519	

Table 9: Relative role of each perturbation or improvement

other are pretty small. Further away from the Moon (than the LLO), the integrator's parameters are less significant for the accuracy and the main importance are the two other bodies, Earth and Sun. We expected the importance of the Earth to rise because the spacecraft is on the edge of Moon's SoI.

5.5 Distant Retrograde Orbit

5.5.1 Reference orbit

The DRO is another star orbit of the decade and is being greatly studied. The DRO, same as the NRHO, is defined in the three-body problem and is computed with the CR3BP model.

If an observer on Earth looks at a spacecraft in a DRO orbit around the Moon, he will see a periodic motion with geometric figure depending on the period of the orbit and the resonant ratio. The DRO orbit can form squares or triangles in a Moon centered inertial frame and a completely different shape in the rotational frame but still closed. DROs are also famous because they are retrograde so the rotation around the Moon is opposite to all other bodies in space.

DROs are really interesting because of their high stability properties and a spacecraft (or asteroid) can stay for years without maneuvers in the same orbit. A DRO was then chosen by NASA for the Artemis I mission in which the Orion spacecraft went into a 14 days period DRO for 6 days [2]. This spacecraft will then be our reference for the DROs. We chose the epoch 29 November 2022 at 4pm and a span of 1 day. This date was chosen because the Artemis I mission presents a lot of small maneuvers during the 6 days in DRO orbit. The period chosen was then free of maneuvers and comprised in one single ephemeris file so that there is no concatenation error. The Orion DRO has a 14 days period and has an apolune of 94 800 km and perilune of 70 100 km. Finally, the computing time on a medium Intel i5 11^{th}G computer is 0.38s for an RMSE accuracy of 417.8m. The initial integration step size before the step size control was of 60s.

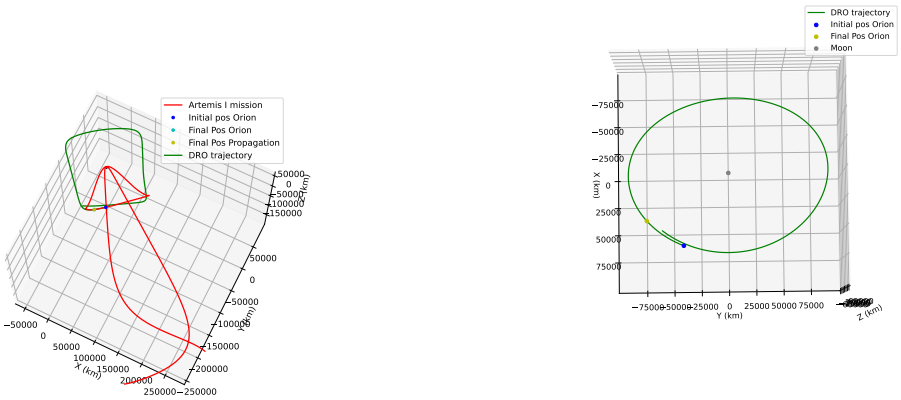

(a) Artemis 1 mission in the inertial frame

(b) Orion's DRO orbit in the rotational frame (14 days)

Figure 12: Artemis 1 mission and its DRO orbit

In Figure 12a, we can see the Artemis 1 mission in the Moon centered inertial frame. We only consider a small part of the full trajectory (in between the initial and final position) and also a small part of the DRO orbit (only 1 day on the 6 total). The green orbit corresponds to the DRO orbit where the Orion spacecraft was before the exit maneuver, and we can observe the almost square shape

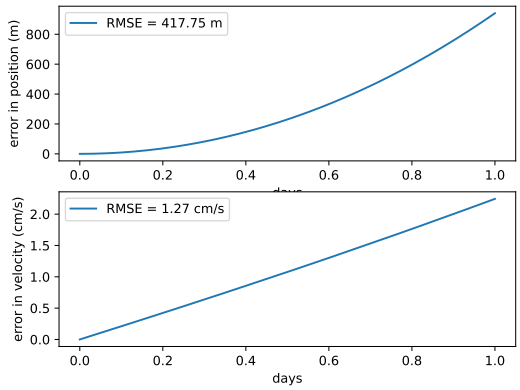

Figure 13: Propagation errors of the Orion

after 28days (2 periods). On Figure 12b, the Orion DRO orbit is represented in the Moon centered rotational frame and is almost closed. A period of a bit less than 14 days can be seen on this figure.

On the Error graph 13, we can see that the position error goes up significantly which may correspond to a lack in the modelling for this specific orbit and this specific part of the orbit. That is why we prefer assessing the orbit on a full period which was not possible here.

5.5.2 Magnitude of each perturbation

To be able to assess the Magnitude of each perturbation for the DRO, we can't use the Orion spacecraft because the span is only 1 day over the 14 days period. Therefore, we took the associated orbit (square shaped) and made it converge from the CR3BP model to the high fidelity model that we use. This was done with the algorithm presented in Section 5.3. Then we studied the amplitude of all perturbations with this similar real DRO trajectory for half a square so 1 period, 14 days (a full square is actually 2 periods).

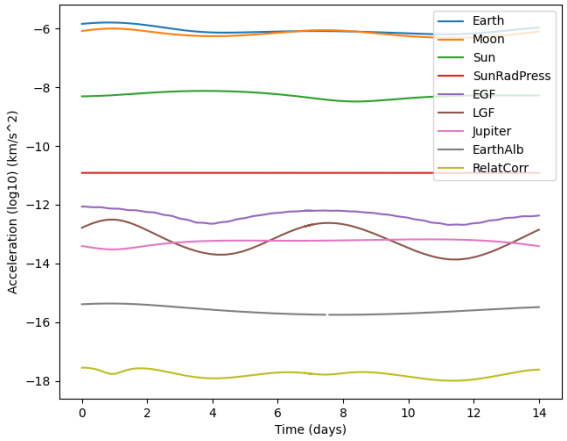

Figure 14: Magnitude of perturbations during a DRO

In Figure 14, we study the accelerations over 1 period so given the geometry, we should see 2 periods of same pattern and that is approximately what we can see for all curbs. Indeed, the DRO is not exactly periodic but close to it, because we are in a high fidelity model. The DRO is stable in a certain domain of evolution.

Similarly to the NRHO, the apolune and perilune are really close to the Moon's SoI so the Earth and Moon's perturbation are around the same order of magnitude. Same for the associated gravity field correction.

The relativistic correction is really low in this situation because of the distance to the Moon, similarly to the NRHO.

5.5.3 Sensitivity analysis

In this section, we are going to remove each perturbation or improvement made and assess the propagator in order to be able to tell what is the relative role of each. Every other perturbation or improvement being similar to the reference.

As a remainder, the reference situation is a DRO on 1 day and the model parameters are the same as for the LLO in section 5.2.3, except for the relative tolerance, which was set to 10^{-7}.

	Reference	10x10 LGF	w/o Earth	w/o Sun	w/o SRP	w/o GRC
RMSE (km)	0.418	0.418	1325	8.932	0.400	0.418
	0x0 EGF	w/o Jupiter	w/o Albedo	ODE45 (RT=10^{-7})	RT of 10^{-6}	
RMSE (km)	0.418	0.418	0.418	0.418	0.418	

Table 10: Relative role of each perturbation or improvement

With Table 10, we can see that removing some perturbation reduces the accuracy except for the SRP. This single anomaly may be due to a integrator positive mistake or to a poor modelling and this will be discussed in the sum up part. The results are quite similar to the NRHO ones, overall we can see that the biggest impact is the Earth attraction then the Sun, the other are really small. Further away from the Moon (compared to the LLO), the integrator's parameters are less significant for the accuracy and the main importance are the two other bodies, Earth and Sun. We expected the importance of the Earth because of the definition of the orbit in the Earth-Moon rotational frame.

5.6 Sum up of the perturbations over all orbits

We are going to summarize here all the previous information on all 4 orbits. To be able to compare information, we are going to consider for each orbit a reference value and consider for each perturbation on this orbit the ratio of the value calculated over this reference value. The reference value will be the error for a 1 day propagation, by linearly adjusting the value if needed (if the period is greater than 1 day for instance).

Orbits	LLO	ELFO	NRHO	DRO
Reference 1 day (m)	104.7	39.5	222	417.8
10x10 LGF	10.9	2.47	≈ 1	≈ 1
w/o Earth	1.94	95.6	7143	3170
w/o Sun	0.93	2.31	64.6	21.3
w/o SRP	0.90	0.94	1.23	0.96
w/o GRC	0.93	≈ 1	≈ 1	≈ 1
0x0 EGF	0.98	≈ 1	≈ 1	≈ 1
w/o Jupiter	1.05	≈ 1	1.03	≈ 1
w/o Albedo	0.87	≈ 1	≈ 1	≈ 1
ODE45 (RT=10^{-7})	1.44	1.32	0.97	≈ 1
RT=10^{-6}	7.16	14.1	1.75	≈ 1

Table 11: Sum up of all perturbations over all orbits

Much information can be retrieved from Table 11. The values for each perturbation help to assess the impact on the orbit. If the ratio is high, it means that the impact is important, because it means that by removing the perturbation, the error increases by a factor of the ratio calculated. Then if it is close to 1 the impact is small and if it is less than 1, it is an anomaly. We can observe multiple anomalies in the table and they can be called such way because, by removing one of the perturbation, we should lose in accuracy and the RMSE should then go up and be greater than 1. Almost all the anomalies are located for the LLO or for the SRP. This shows that there was either a positive integration error or that the modelling has to be improved. For instance, the modelling of the SRP supposes a circular

section for the satellite and this table could mean that this modelling lacks accuracy. These anomalies might also be attributed by the reference orbits (i.e., the accuracy & precision) and the short time span of the orbits (only one day). However, we couldn't perform wide-scale analysis due to the limitation of reference orbits, that have to be existing lunar mission. For the anomalies on the LLO orbit, we can observe that the two last parameters vary a lot, and they correspond to the integrator's impact. Therefore the orbit can be considered as hard to integrate, and the strong and complex lunar gravity field can be an explanation, so that we understand better the positive and small anomalies. However, the ELFO orbit also present this high variation property for the integration related parameters, but without a lot of anomalies. The high amplitude of the complex LGF in LLO remains then the main candidate.

Moreover, in terms of the 1 day reference, the ELFO has the best accuracy, better than the LLO then the NRHO and finally the DRO. For the comparison between LLO and ELFO, we can argue that the closer to the Moon the more impact has the complex lunar gravity, and that would explain why the LLO is less accurate. Then for the NRHO and DRO, we observe the great influence of the Earth because they are 3 body problem orbits. They are then more complex and the propagation is harder which explain the gap with the 2 first orbits. However the DRO is known to be a much more stable orbit than the NRHO so we would have expected it to have a better accuracy than the NRHO. We could explain it by the quality of the DRO reference. Indeed, it was only a 1 day sample instead of the full orbit (14 days) and there were many maneuvers and discontinuities on the trajectory that we avoided by choosing a clean segment but little control maneuvers could still be in the chosen segment. In addition, we can observe that the lunar gravity field's influence improves from LLO to DRO, and the influence of the Earth decreases which is explained by the growing distance to the Moon.

Lastly, we can see that the Earth albedo, the Jupiter attraction, the EGF, the GRC and even the SRP have always really low impact on all orbits except the LLO which is more complex. This table 11 can then be used to assess which force/perturbation can be removed in order to be cost efficient in computational time if the propagation has to be done on a really long period of time for instance.

6 Mission design

The refined propagator was then incorporated into a mission design tool. The tool provides 5 modes that can be arranged in a sequential to form a specific mission.

Among those modes, we have a free propagation, a propagation with added maneuver at initial time, a Lambert transfer propagation, an optimized Lambert transfer and finally a 3-body-problem orbit convergence algorithm.

The first mode is then a free propagation with the propagator given a specific span. Then we have the propagation with added maneuver: the maneuver, at initial point, allows to reach the desired orbit with an impulsive change of velocity. It needs a span and a target orbit in input. This mode is particularly useful in the end of a Lambert transfer where we want to boost to the desired orbit. The third mode is then the Lambert transfer between two points, the algorithm used comes from an already developed, really fast and robust solver [19]. It also needs a span and a target orbit. Then with the fourth mode, we implemented an optimized Lambert solver given the previous solver, the algorithm is presented in the next part. It needs a target orbit and a guess for the 3 parameters defined in the related section. Lastly we implemented on the fifth mode a trajectory convergence algorithm for 3-body-problem orbits (DROs and NRHOs) also developed in next sections. This last mode only needs the period of orbit, which for a 3-body-problem is the periodic time for which the trajectory repeats in the rotational frame and there is usually no periodicity of the trajectory in the inertial frame.

The following section will develop the algorithms used for the 2 last modes. The two proposed algorithm do not pretend to be optimal but they are a good first solution to the problem that could be further refined if needed.

6.1 Lambert problem optimizer algorithm

The problem we want to solve here is what is the optimized way to go from one orbit to another. This problem is very relevant to the study of 3BP orbits because the Gateway space station is in an NRHO and DV(Delta Velocity)-efficient transfers will have to be studied from different orbits in the cis-lunar domain to the Gateway NRHO.

To solve this problem, we are using the Matlab function fminsearch, a nonlinear programming solver that uses a simplex search method. The objective function to minimize is the sum of the DVs of the boost to enter the transfer orbit and the boost to join the second orbit, with the addition of a penalty term. This punishment term is proportional to the norm of the difference between the Lambert target (second orbit) and the resulting propagation after the Lambert calculation, it is basically the error between the target and the final position. The punishment factor was chosen as 1 km/s every 2 km of error. We have then 3 parameters to optimize which are the point of departure from the first orbit, then the span of transfer and finally the point of arrival on the second orbit. To define a position on an orbit, we use a propagation time from a reference position on the orbit. We then have 3 parameters, 2 times defining the position on the departure and arrival orbits and a time-span for the travel time between the two points.

As an example, we tried to optimize the transfer from the Gateway NRHO to an ELFO in Figure 15. The initial situation had 4.470 km/s of total DV and an error of 251 km whereas the final situation has only 0.816 km/s of DV and 122 km of error.

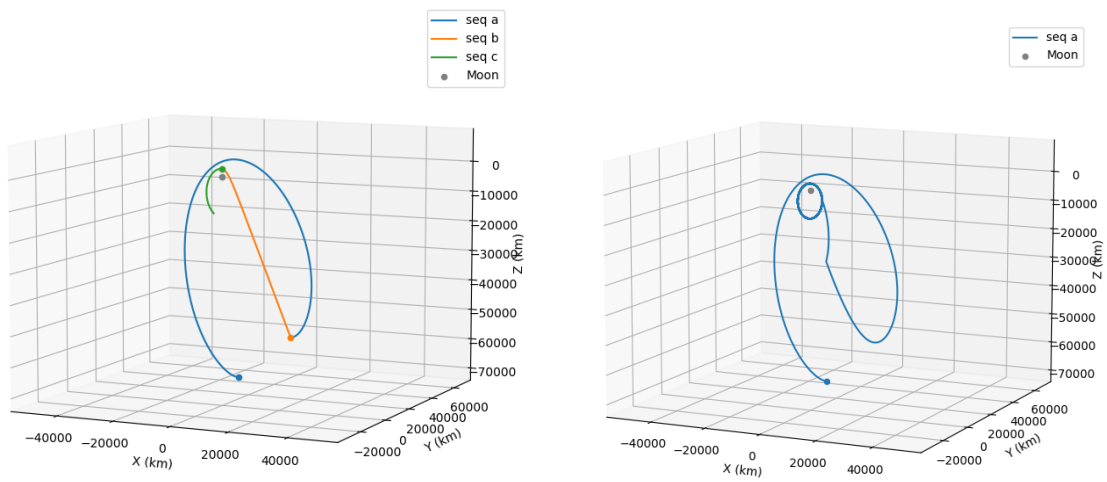

(a) Initial situation

(b) Converged situation

Figure 15: Optimization of a Lambert transfer between the Gateway NRHO and an ELFO

6.2 3BP Orbits optimization algorithm

When studying 3-body-problem (3BP) orbits (for instance DROs and NRHOs), after fitting a simplified model trajectory (calculated in the CR3BP) on an ephemeris model (as in section 3.2.3), the trajectory is not in a 3BP orbit anymore. However, this fitting gives us a good first guess to converge to an high precision model 3BP orbit.

In order to improve our initial guess, we use the Matlab function fsolve, a nonlinear system root solver which uses a Levenberg-Marquardt algorithm in our case, a non linear least square algorithm. The objective function we chose to nullify is composed of multiple similar parts. The first one is the difference between the original state and the state reached after a one-period propagation, and the other parts are the same but with a multiple-periods propagation. If this objective function is nullified, the same state will be reached after a propagation and the motion will be periodic. The use of the multiple period part is to achieve a better convergence because the zero is never exactly reached. We can choose the number of period taken into account depending on the stability of the solution.

However, the 3BP orbits are not periodic in the inertial frame but in the rotational one, so the conversion presented in 3.2.3 has to be done. Therefore, the decision variables are the 6 variables corresponding to the original state and we have a system of 6*n equations for the objective function, 6 for each periodicity after i period for i from 1 to n, n being the number of period taken into account. We use section 3.2.3 for the conversion on the two first lines and f is objective function.

$$
\begin{aligned}
&\vec{MS}_{[R]}(t) = M_{RI}^{-1}(t).\vec{MS}_{[I]}(t) \\
&\vec{V}_{S/M[R]}(t) = M_{RI}^{-1}(t).\left(\vec{V}_{S/M[I]}(t) - \vec{\Omega}_{R/I}(t) \times \vec{MS}_{[I]}(t)\right) \\
&f\begin{pmatrix} \vec{MS}_{[I]}(t=0) \\ \vec{V}_{S/M[I]}(t=0) \end{pmatrix} = \begin{cases} \forall i \in [\![1;n]\!] \\ \vec{MS}_{[R]}(t=i\cdot T) - \vec{MS}_{[R]}(t=0) \\ \vec{V}_{S/M[R]}(t=i\cdot T) - \vec{V}_{S/M[R]}(t=0) \end{cases}
\end{aligned} \tag{37}
$$

We will show 2 examples, one with a NRHO close to the Gateway and the other with a DRO close to the one used by the ORION spacecraft during the Artemis I mission. First of all, the Gateway NRHO has a period of about 6.5 days, an perilune altitude of 1500 km and an apolune of 70 000 km. We chose then a NRHO with a similar period of 6.65 days and similar apolune and perilune and we want to make it converge to an accurate ephemeris trajectory on the random chosen date of 1 January 2024 (as if we were designing a mission). After retrieving the initial data of this similar orbit in the CR3BP on the JPL database [20], we can fit the initial state to the ephemeris model, accordingly to 3.2.3, and initialise with it the previous optimization algorithm.

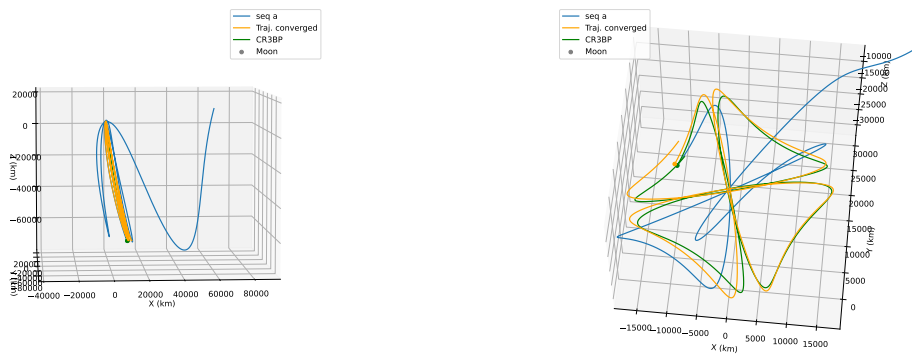

(a) Moon centered rotational frame

(b) Moon centered inertial frame

Figure 16: Optimized NRHO trajectory

On Figure 16, we have the CR3BP trajectory in green, the blue trajectory corresponds to the propagation of the fitted CR3BP trajectory (so the initial guess) and the orange trajectory is the result of the optimization until 3 periods. The computing time was about 75 s on a medium i5 computer with 31 function calls. We can see a clear improvement from the blue trajectory, that goes out of NRHO after 4 periods, and the orange one which is concentrated around the green trajectory in the rotational frame, and that follows the pattern of the CR3PB trajectory in the inertial one. The orange trajectory is not exactly similar to the green one but the change of initial state allowed the blue trajectory to turn into an orbit (orange) with similar properties as the green one.

The second example will be with a DRO close to the one used in the Artemis I mission. This orbit had a period of around 14 days so we chose a CR3BP DRO with this period span in the JPL database [20]. Similarly, we fit the data and initialise the optimization.

For the same number of period than the NRHO (n=3), in this case the optimization does not converge well. So the convergence was reached on Figure 17 for n=2. This hard convergence may be due to a bad initial guess and because of the long period of 14 days. Therefore a convergence with n=3 can be processed after the first convergence if a better solution is needed.

Similarly with the NRHO, the initial guess (blue) goes out of the DRO after only some days. After half a period (so a quarter square in inertial) the orange trajectory (optimized) is well closed in the rotational frame and shares the same characteristics as the CR3BP square in the inertial frame.

Those two examples show how to use the algorithm and what to do if the convergence is not reached.

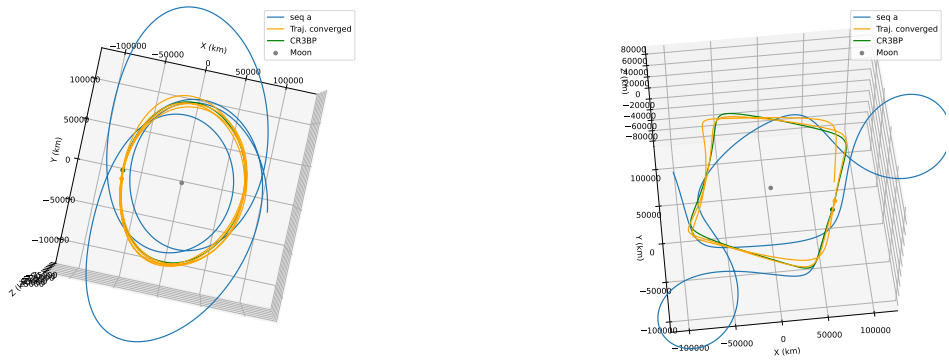

(a) Moon centered rotational frame

(b) Moon centered inertial frame

Figure 17: Optimized DRO trajectory

7 Conclusion

During this study, we developed a high accuracy propagator, we provided a detailed modeling of all forces and perturbations, and we implemented the propagator into an open source mission design tool. The detailed modeling and comprehensive explanation of algorithms and methods were done in order to allow an easy understanding and a fast appropriation of the tool to other studies. An assessment of the propagator on different interesting orbits was done which gives information on the propagator and also methods for the user to assess it on his own.

We discussed about how the modelling could be improved in the third section (IV) and how different modifications on the integration methods for instance are of prime importance for the sake of the propagator's accuracy (IV). Those are the ways to go in order to further improve the propagator depending on the purpose of the improvement. This purpose can be motivated by the sum up part on the results over different orbits (V). Then the algorithms and use of the mission design tool were presented (VI).

We chose to assess the propagator with real ephemeris data from spacecraft in the orbits of interest but we could also have chosen to compare the accuracies with widely used mission design tools like STK (Systems Tool Kit from Ansys) or GMAT (General Mission Analysis Tool from NASA). We also chose to implement specific optimization techniques for specific mission design problems like the optimized Lambert and the optimized 3-body-problem trajectory.

We hope that this open source tool HALO will be used in other researches and we encourage to further developed it.

8 Acknowledgement

I would like to acknowledge the UNSW Faculty of Engineering's funding support for my research in Australia. I would also like to acknowledge the work of Enio Condoleo and his Lunar High Precision Orbit Propagator which was the base work for this study.

8.1 Declaration of competing interest

The authors have no competing interests to declare that are relevant to the content of this article.

9 References

References

[1] Lee D. Gateway Destination Orbit Model: A Continuous 15 Year NRHO Reference Trajectory, 2019.

[2] Batcha AL, Williams J, Dawn TF, Gutkowski JP, Widner MV, Smallwoodk SL, Killeen BJ, Williams EC, Harpold RE. Artemis I trajectory design and optimization. *AAS/AIAA Astrodynamics Specialist Conference*, 2020.

[3] Matsumoto Y, Nakamura R, Kikuchi J, Ueda S. Design of Elliptical Lunar Frozen Orbit Considering Lunar J2 Perturbations. *American Institute of Aeronautics and Astronautics*, 2024.

[4] Gardner T, Cheetham B, Clarkson M. CAPSTONE: Mission Updates and Ongoing Efforts at the Moon, 2023.

[5] Dombard AJ, Hauck SA, Balcerski JA. On the origin of mascon basins on the Moon (and beyond). *American Geophysical Union*, 2013.

[6] Hughes SP, et al. Verification and validation of the general mission analysis tool (GMAT). *AIAA/AAS astrodynamics specialist conference*, 2014.

[7] Montenbruck O, Gill E. *Satellite Orbits Models, Methods and Applications*, Springer, 2000.

[8] Mocnik FB, Westerholt R. The effect of tectonic plate motion on georeferenced long-term global datasets. *International Journal of Applied Earth Observation and Geoinformation*, 2021.

[9] Condoleo E. Lunar High precision Orbit Propagator. Matlab File Exchange, 2017.

[10] Bertone S, Arnold D, Girardin V, Lasser M, Meyer U, Jäggi A. Assessing Reduced-Dynamic Parametrizations for GRAIL Orbit Determination and the Recovery of Independent Lunar Gravity Field Solutions. *American Geophysical Union*, 2021.

[11] FShampine L, Reichelt MW. The Matlab ODE suite. *SIAM Journal on Scientific Computing, Volume 18, Issue 1*, 1997.

[12] Dormand J, Prince P. A family of embedded Runge-Kutta formulae. *Journal of Computational and Applied Mathematics, Volume 6, Issue 1*, 1980.

[13] Verner JH. Numerically Optimal Runge–Kutta Pairs with Interpolants. *Numerical Algorithms 53, no. 2–3*, 2010.

[14] Shampine LF, Gordon MK. Computer Solution of Ordinary Differential Equations: the Initial Value Problem. *San Francisco : W. H. Freeman*, 1975.

[15] Information on https://naif.jpl.nasa.gov/naif/index.html.

[16] Information on https://naif.jpl.nasa.gov/naif/data_archived.html.

[17] Mesarch MA. An Observational Approach to Low Lunar Frozen Orbit Design. *AAS/AIAA Astrodynamics Specialist Conference*, 2023.

[18] Information on https://science.nasa.gov/mission/clementine/.

[19] Izzo, Lancaster, Blanchard, Gooding, Oldenhuis R. Robust solver for Lambert's orbital-boundary value problem.

[20] Information on https://ssd.jpl.nasa.gov/tools/periodic_orbits.html#/intro.

9.1 Author biography

Quentin Granier is a research associate for the Australian Centre for Space Engineering Research (ACSER) in University of New South Wales (UNSW). He is a French engineering student from CentraleSupélec with a general bachelor in engineering and specialising in mission analysis and/or guidance, navigation and control during is master. This research was an internship and 4-months project with ACSER.

Yang Yang is currently a Lecturer with the School of Mechanical and Manufacturing Engineering, University of New South Wales (UNSW), Sydney, Australia. His PhD was awarded from Northwestern Polytechnical University, Xi'an China. His research interests include astrodynamics, advanced estimation, space navigation, space situational awareness and GNSS positioning & navigation.

Andrew Dempster received the B.E. and M.Eng.Sc. degrees from UNSW in 1984 and 1992, respectively, and the Ph.D. degree in efficient circuits for signal processing arithmetic from the University of Cambridge in 1995.,He is currently the Director of the Australian Centre for Space Engineering Research (ACSER) in University of New South Wales (UNSW). He has published in the areas of arithmetic circuits, signal processing, biomedical image processing, satellite navigation, and space systems. He has six patents on new location technologies and space systems.